ACS OMEGA

Open Access

http://pubs.acs.org/journal/acsodf

Article

Magnetic UiO-66-NH_2 Core–Shell Nanohybrid as a Promising Carrier for Quercetin Targeted Delivery toward Human Breast Cancer Cells

Mozhgan Parsaei and Kamran Akhbari*

Cite This: *ACS Omega* 2023, 8, 41321–41338

Read Online

ACCESS | Metrics & More | Article Recommendations | Supporting Information

ABSTRACT: In this study, a magnetic core–shell metal–organic framework (MOF) nanocomposite, Fe_3O_4-COOH@UiO-66-NH_2, was synthesized for tumor-targeting drug delivery by incorporating carboxylate groups as functional groups onto ferrite nanoparticle surfaces, followed by fabrication of the UiO-66-NH_2 shell using a facile self-assembly approach. The anticancer drug quercetin (QU) was loaded into the magnetic core–shell nanoparticles. The synthesized magnetic nanoparticles were comprehensively evaluated through multiple techniques, including FT-IR, PXRD, FE-SEM, TEM, EDX, BET, UV–vis, ZP, and VSM. Drug release investigations were conducted to investigate the release behavior of QU from the nanocomposite at two different pH values (7.4 and 5.4). The results revealed that QU@Fe_3O_4-COOH@UiO-66-NH_2 exhibited a high loading capacity of 43.1% and pH-dependent release behavior, maintaining sustained release characteristics over a prolonged duration of 11 days. Furthermore, cytotoxicity assays using the human breast cancer cell line MDA-MB-231 and the normal cell line HEK-293 were performed to evaluate the cytotoxic effects of QU, UiO-66-NH_2, Fe_3O_4-COOH, Fe_3O_4-COOH@UiO-66-NH_2, and QU@Fe_3O_4-COOH@UiO-66-NH_2. Treatment with QU@Fe_3O_4-COOH@UiO-66-NH_2 substantially reduced the cell viability in cancerous MDA-MB-231 cells. Cellular uptake and cell death mechanisms were further investigated, demonstrating the internalization of QU@Fe_3O_4-COOH@UiO-66-NH_2 by cancer cells and the induction of cancer cell death through the apoptosis pathway. These findings highlight the considerable potential of Fe_3O_4-COOH@UiO-66-NH_2 as a targeted nanocarrier for the delivery of anticancer drugs.

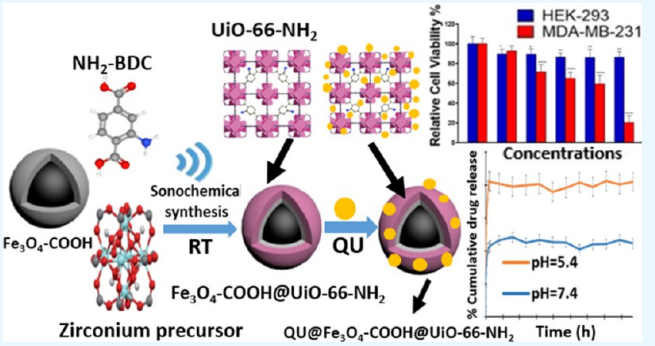

1. INTRODUCTION

A wide range of diseases mainly caused by oxidative stress, including cancer, atherosclerosis, and coronary heart disease, are potentially prevented by dietary antioxidants including polyphenolic compounds. Quercetin (QU; 2-(3,4-dihydroxyphenyl)-3,5,7-trihydroxy-4H-chromen-4-one with a molecular size of 4.24–7.11 Å) is a polyphenol compound with broad distribution across various herbs, vegetables, leaves, fruits, seeds, red wine, tea, coffee, beer, fruit juice, and several medicinal plants.[1−9] Additionally, the supplement is available commercially, while the dose of 1 g per day of oral administration is considered safe.[10] Quercetin is characterized by a 15-carbon skeleton comprising two benzene rings (A and B) within its structure connected via an oxygen-containing pyrene ring (C) hydroxylated in positions 3, 5, 7, 3′, and 4′ (Figure S1 in the SI). Quercetin has exhibited potential for various pharmacological applications, including antioxidant, antimicrobial, antineoplastic, anti-inflammatory, neuroprotective, antiaging, antiallergic, antiproliferative, antidiabetic, and anticancer activities.[11−23] Investigations conducted in vitro and in vivo have validated the anticancer properties of quercetin.[24−27] Several cancer cell lines, including breast cancer, human ovarian cancer, lung cancer, human colon cancer, and human gastric cancer, are shown to be inhibited by quercetin.[28−32] Moreover, quercetin can reduce multidrug resistance of cancer cells[33] and enhance the antitumor properties of the drugs.[34] Due to antioxidant pharmacophores in its structure, quercetin exhibits a robust affinity for binding transition-metal ions and demonstrates effective scavenging of free radicals.[35] A valuable feature of its structure is the existence of catechol at position C3 and the OH group at position C3 enabling it to scavenge free radicals quite effectively.[36] Inhibition of lipid peroxidation is strongly enhanced by a 3′,4′-catechol structure in the B ring. The peroxyl radical, superoxide radical, and peroxynitrite radical are scavenged most effectively by quercetin due to this property.[37] The bioactivity of quercetin primarily stems from its capacity to stimulate and augment the endogenous defense mechanisms

Received: July 6, 2023
Accepted: October 3, 2023
Published: October 24, 2023

against free radicals.[38] However, quercetin's poor bioavailability, resulting from low water solubility (2.15 μgmL^{-1} at 25 °C) and chemical instability in neutral and alkaline environments, limits its anticancer effect.[39,40] It has been demonstrated that applying drug delivery systems can overcome this problem. Therefore, a wide variety of drug delivery systems (DDSs) have been employed as quercetin carriers, including micelles, hydrogels, lipid nanoparticles, metal and metal oxide nanoparticles, dendrimers, polymeric compounds, carbon nanotubes, chitosan nanoparticles, graphenes, inorganic silica, polymeric gels, albumin, and metal−organic frameworks.[41−54] The unique architecture of nanocarrier-based platforms considerably overcomes the limitation of conventional drug delivery methods, including high toxicity, poor specificity, and drug resistance induction.[55] Metal−organic frameworks (MOFs) consist of a distinctive class of porous materials characterized by the presence of robust bonding interactions between an inorganic core and polydentate bridging organic linkers. In contrast to conventional porous materials, MOFs offer several notable advantages, including high specific surface area and porosity, low crystal density, tunable pore sizes, multifunctionality (owing to the wide variety of possible arrangements of metals and ligands), enabling precise modulation of their physicochemical properties for specific applications, and favorable biocompatibility. Recently, a variety of applications of these compounds have been documented in different fields, including catalysts, sensing, gas storage, antibacterial properties, and especially drug delivery.[56−66] The fascinating characteristics of MOFs, including exceptional stability, significant surface area, controllable functionalization, and the ability to incorporate functional groups, have rendered them highly appealing for utilization as carriers in drug delivery applications.[67−71] The encapsulation of quercetin into the UiO-66 structure provided a synergetic dual sensitizing effect, demonstrating a loading of 20.7%.[72] Another study found that FA-BSA/CuS@ZIF-8 has about 24% drug-loading capacity toward quercetin.[73] According to recent research, UiO-66 and its functional analogues with $-NO_2$ and $-NH_2$ groups could effectively deliver quercetin.[74] According to this study, UiO-66, UiO-66−NO_2, and UiO-66−NH_2 demonstrated 32.9, 37.0, and 40.1% drug-loading capacities, respectively. An effective drug delivery system consists of a manageable process for controlling time, dosage, and release site. Targeting anticancer drugs to tumor tissues reduces remarkably the side effects, enhances the curative effects, and improves local drug concentration. Therefore, targeting drug delivery system (TDDS) is employed to selectively deliver anticancer drugs to tumor tissues. Endogenous stimuli (pH, redox, enzymes) or exogenous stimuli (pressure, humidity, magnetic fields, ultrasound irradiation, glucose level, ions, light, temperature) can trigger a controllable drug release.[75] In these regards, incorporating magnetic nanoparticles into MOFs with the potential for use in magnetic-based diagnostic approaches and as an effective technique for carrying drugs directly to a specific site through external magnetic fields has attracted much attention.[76−80] This desired targeting behavior limits drug spreading in the general circulation and reduces side effects. Moreover, superparamagnetic nanoparticles can reduce the spin−spin T_2*-relaxation time during magnetic resonance imaging (MRI), enhancing contrast in T_2-weighted images using magnetic nanoparticles.[81,82] Furthermore, magnetic fields as external stimuli can also induce the release of drugs from magnetic nanocarriers.[83,84] Numerous reports are available on magnetic drug delivery systems; however, most of them suffer from several limitations such as low stability, swelling, and insignificant controllability.[85−87] Therefore, the design and construction of materials with a magnetic core as a drug delivery system that can overcome the disadvantages mentioned above would be valuable. A MOF-based magnetic nanocomposite was prepared by the incorporation of Fe_3O_4 nanorods in $Cu_3(BTC)_2$ nanocrystals (BTC; benzene-1,3,5-tricarboxylate). After encapsulation within the Fe_3O_4@$Cu_3(BTC)_2$ nanocomposite, the release of sodium nimesulide, an anticancer drug, was observed to occur over a period of 11 days in a physiological saline solution.[68] In another study, Fe_3O_4@ZIF-8, a pH-sensitive MOF, was used to fabricate a delivery system using Fe_3O_4 magnetic particles for heparin delivery.[88] In a recent investigation, the solvothermal synthesis of amine-functionalized UiO-66 with magnetic properties for the purpose of delivering oxaliplatin was reported. The synthesis process involved heating a synthesis medium comprising DMF at 80 °C for a duration of 37 h.[89]

Among MOFs, zirconium-based MOFs demonstrated high levels of biocompatibility, biodegradability, and a remarkable degree of chemical and thermal stability.[90,91] MOFs constructed from carboxylate linkers and cationic zirconium clusters, such as UiO-66 and derivatives, have great potential applications as drug carriers owing to their high surface areas, remarkable aqueous stability, and high loading capacity.[92−108] Moreover, zirconium (Zr) exhibits minimal toxicity, as demonstrated by its low lethal dose (LD_{50}) of 4.1 g/kg in rats when administered as zirconyl acetate. Furthermore, it is worth noting that the human body naturally contains approximately 300 mg of Zr, with a daily ingestion rate estimated to be around 3.5 mg per day.[109] 2-Aminobenzene-1,4-dicarboxylic acid, as an exogenous organic linker, showed LD_{50} = 5 g kg^{-1}.[110] In acidic conditions, MOFs degrade and collapse, releasing their encapsulated contents at tumor sites as a result of the protonation of the carboxylate units and surface functionality.[111] Within the UiO-66 family, there are two distinct types of pore cages, tetrahedral and octahedral, exhibiting respective diameters of 7.4 and 8.4 Å.[94] Amine-functionalized zirconium-based dicarboxylate MOF, UiO-66-NH_2, has been investigated in many studies as a nanocarrier for incorporation and release of drug molecules.[112−117] The NH_2 functional group improves the interaction between the drug molecules and MOFs, providing enhanced drug binding, loading, and release characteristics.[118]

Significant endeavors have been made to enhance the structural characteristics and properties of MOFs;[119−128] however, their synthesis suffers from some disadvantages such as needing to use high temperatures, aggressive reagents, and long reaction times. A variety of alternative routes have been developed, including sonochemical, mechanochemical, spray-drying, electrochemical, and microwave-assisted synthesis.[129−133] Recently, the sonochemical process including ultrasonic radiation as a reactivity inducer has been introduced as a sufficient substitute for traditional MOF synthesis using strong acids.[134−137] This method offers several advantages, including being rapid, economical, reproducible, and eco-friendly. Moreover, using ultrasounds during MOF preparation accelerates nucleation; therefore, crystallization takes less time at low reaction temperatures and ambient pressures. As a result, smaller and more uniform particles are obtained from this method compared to solvothermal synthesis.[138] Additionally, the conventional synthesis of magnetic UiO-66-NH_2

https://doi.org/10.1021/acsomega.3c04863
ACS Omega 2023, 8, 41321−41338

involves using DMF as a solvent, which is evaluated as hazardous due to its chronic toxicity.[139−143] Therefore, the identification of a medium with higher safety standards to replace it is fundamental.[144]

As a part of our investigation of applications of MOF structures in drug delivery systems,[145−150] we have investigated the sonochemical fabrication of core−shell magnetic zirconium-cluster-based MOF, Fe_3O_4@UiO-66-NH_2, avoiding the use of toxic solvents, aggressive reagents, or high temperatures, and evaluated suitability of the synthesized nanocomposite as a drug delivery system by encapsulating quercetin, an anticancer agent, within its structure.

2. EXPERIMENTAL SECTION

2.1. Materials and Methods. All chemicals used were analytical grade and employed as received without further purification and were purchased from Sigma-Aldrich or Merck. The powder X-ray diffraction (PXRD) analyses were conducted under ambient conditions utilizing a Rigaku Ultima IV diffractometer, employing monochromatic Cu Kα radiation (λ = 1.54056 Å) from 5 to 50° with a step size of 0.02°. The Mercury software was employed to perform simulations of X-ray diffraction (XRD) powder patterns, utilizing the crystallographic data obtained from single-crystal analysis. A Rayleigh spectrophotometer was employed to acquire UV−vis spectra between 300 and 550 nm. FT-IR spectra in the range of 400−4000 cm^{-1} were acquired utilizing a PerkinElmer Spectrum One FT-IR spectrometer equipped with ATR (attenuated total reflection) mode and DTGS (deuterated triglycine sulfate) detectors. The spectra were recorded with a resolution of 4.0 cm^{-1} and an accumulation of 16 scans. Fluorescence imaging was performed with an Optika B500TiFL microscope. The TEM (transmission electron microscopy) images were captured by employing a Philips EM 208S apparatus. SEM images with gold coating were obtained by using a TESCAN MIRA3 scanning electron microscope. An Oxford instrument detector was employed to conduct EDX analyses. Zeta potential (ZP) measurements were carried out in an aqueous medium using a Malvern ZS90 instrument from the ZetaSizer Nano Series. Magnetic properties were investigated by utilizing a vibrating sample magnetometer (VSM-7300, Meghnatis Daghigh Kavir) at room temperature. To calculate surface area (BET), N_2 adsorption and desorption isotherms at 77 K were determined using the Belsorp mini II apparatus. Before characterization, a vacuum degassing treatment using a BELPREP VAC apparatus was employed to activate all samples for a duration of 24 h under high-vacuum conditions.

2.2. Material Synthesis. *Synthesis of Fe_3O_4-COOH Magnetite Nanoparticles.* Magnetite nanoparticles were synthesized following the procedures given in previous literature with some modifications.[151] Various factors influence the shape and the size of magnetite nanoparticles, including salt concentrations and molar ratios, nature and concentrations of base solution, and temperature and reaction time. For the synthesis of nanoparticles of suitable size and uniformity, different concentrations of ferric salt and trisodium citrate (Na_3Cit) were used until the optimal concentration was achieved (Table S1 in the SI). Optimum synthesis was achieved by dissolving $FeCl_3.6H_2O$ (8 mmol, 0.64 g) and Na_3Cit (1.36 mmol, 0.32 g) in ethylene glycol (EG; 20 mL). With stirring, sodium acetate (NaOAc; 1.2 g) was then added. Following 30 min of vigorous stirring, the mixture was placed in a stainless-steel 100 mL Teflon-lined autoclave. Following a heat treatment at 200 °C for a duration of 12 h, the autoclave was subjected to a gradual cooling process until the ambient temperature. The resulting black magnetite was isolated through magnetic separation, followed by multiple washings in deionized water and ethanol and drying in a vacuum oven at 60 °C.

Synthesis of Zirconium Precursor Based on Methacrylic Acid. Zirconium precursor ($Zr_6O_4(OH)_4(OMc)_{12}$) was synthesized based on procedures from previous literature with some modifications.[152,153] It was prepared by reacting methacrylic acid with zirconium propoxide ($Zr(PrO)_4$, 70% (w/w) in *n*-propanol). A mixture comprising 1.4 mL of methacrylic acid, 2 mL of $Zr(PrO)_4$ solution, and a drop of water was prepared. The resulting solution was subjected to stirring for 10 min using a magnetic stirrer in a nitrogen atmosphere. Subsequently, the solution was left undisturbed overnight at room temperature, leading to the crystallization of the zirconium precursor from the solution during this period. Afterward, the colorless solid was filtered, followed by thorough washing with i-propanol and subsequent room-temperature vacuum drying (yield: 90% based on methacrylic acid).

Sonochemical Synthesis of Fe_3O_4-COOH@UiO-66-NH_2. Fe_3O_4-COOH@UiO-66-NH_2 was synthesized using a modified version of the approach reported in the literature.[154] The layer-by-layer (LBL) assembly method was employed in the fabrication process. Initially, magnetic nanoparticles (100 mg) were dispersed in 40 mL of an ethanol dispersion containing the Zr-cluster precursor ($Zr_6O_4(OH)_4(OMc)_{12}$; 10 mg). Ultrasonication was performed on the obtained mixture at room temperature for a duration of 15 min. The product obtained was collected through a magnet and rinsed three times with ethanol. Subsequently, an ethanol solution (40 mL) of 2-aminobenzene-1,4-dicarboxylic acid (2-aminoterephthalic acid; NH_2-BDC; 28 mg) was added, followed by another 15 min of ultrasonication at ambient temperature. The resulting mixture was washed three times and separated using a magnet, thus accomplishing the first layer-by-layer self-assembly process. The described procedure was repeated a total of 20 times, following the same steps as those described earlier, resulting in the desired generation of UiO-66-NH_2 on the surface of Fe_3O_4 nanoparticles. The ultimate core−shell nanocomposite (Fe_3O_4-COOH@UiO-66-NH_2) was attained through the process of vacuum drying at ambient temperature in a vacuum oven. The synthesis of UiO-66-NH_2 nanoparticles was accomplished in accordance with a previously documented procedure, serving as a basis for comparison in the present study.[74]

2.3. Drug Loading. Quercetin was loaded into a magnetic MOF, Fe_3O_4-COOH@UiO-66-NH_2, by a typical immersion method. 100 mg of Fe_3O_4-COOH@UiO-66-NH_2 was added to the solvated QU (100 mg) in ethanol (20 mL), and the mixture was subjected to stirring for a duration of 48 h at ambient temperature. Following the loading of QU, the solid material was separated utilizing a magnet and subsequently subjected to overnight vacuum oven drying at room temperature to eliminate residual solvent. A UV−vis calibration curve of QU in ethanol, based on absorbance at λ = 374 nm, was used to calculate drug-loading amounts (Figure S2 in the SI). Using the following formula, the drug-loading capacity (DLC) and drug-loading encapsulation efficiency (DLE) were calculated

https://doi.org/10.1021/acsomega.3c04863
ACS Omega 2023, 8, 41321−41338

Scheme 1. Synthesis of QU@Fe_3O_4-COOH@UiO-66-NH_2

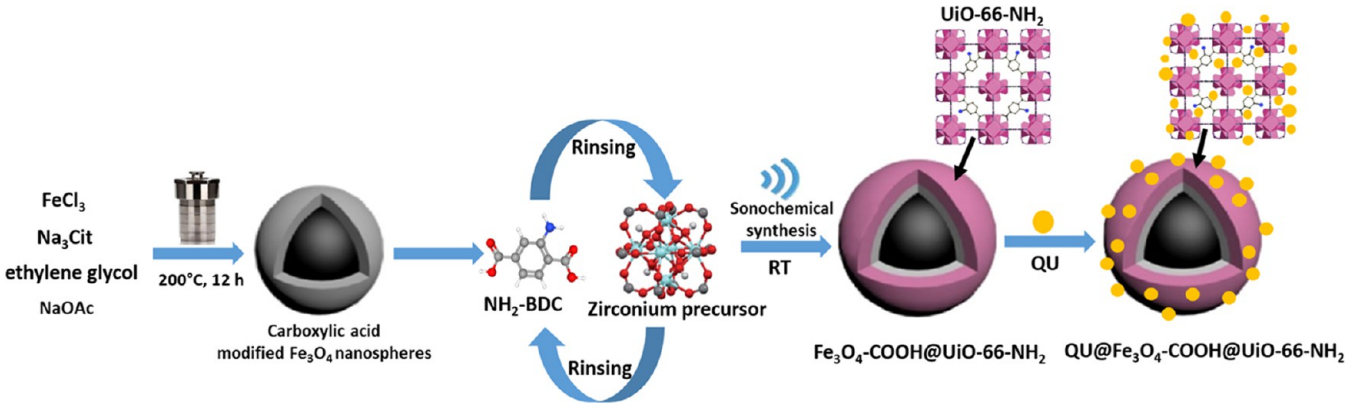

$$\text{DLC (wt \%)} = \frac{\text{weight of loaded QU}}{\text{total weight of QU@Fe}_3\text{O}_4\text{-COOH@UiO-66-NH}_2} \times 100 \quad (1)$$

$$\text{DLE (wt \%)} = \frac{\text{weight of loaded QU}}{\text{total weight of feeding QU}} \times 100 \quad (2)$$

2.4. In Vitro Drug Release Studies. The release behavior of QU@Fe_3O_4-COOH@UiO-66-NH_2 nanoparticles was investigated in buffered media solution (PBS) with different pH values (pH = 7.4 and 5.4) at 37 °C based on the calibration curve of QU in PBS (Figure S3 in the SI). In vitro drug release experiments were performed by suspending QU@Fe_3O_4-COOH@UiO-66-NH_2 (5 mg) in PBS solutions (30 mL) with gentle shaking (80 rpm). At specified time intervals, a 1 mL portion of the released solution was collected and the same volume of fresh phosphate-buffered saline (PBS) solution was added to maintain the volume of the solution constant. The drug concentration in the removed PBS solution was measured by utilizing a UV−visible spectrophotometer at a wavelength of 374 nm, enabling the determination of the drug concentration within the solution under investigation. The cumulative release of the drug was determined by analyzing the concentration of quercetin (QU) in the solution at regular intervals, allowing for the estimation of drug release over time. According to the data acquired, the time-dependent accumulation of drug release was calculated at pH values of 5.4 and 7.4. The corrected concentration of QU and the percentage of drug release were calculated as follows

$$C_c = C_t + \frac{v}{V}\sum_{0}^{t-1} C_c \quad (3)$$

$$\text{drug release (\%)} = \frac{M_R}{M_L} \times 100\% \quad (4)$$

In eq 3, the adjusted concentration of quercetin (QU) at time t is denoted as C_c, while C_t represents the measured concentration at the same time point. The equation incorporates the volume of the extracted sample (v) and the volume of the released solution (V). Moreover, M_R and M_L signify the amounts of drug released and loaded, respectively (eq 4).

2.5. Cell Culture and MTT Assay. The MDA-MB-231 and HEK-293 cell lines were obtained from the Pasteur Institute in Tehran, Iran. These cell lines were cultured in RPMI-1640 media supplemented with 10% fetal bovine serum (FBS), L-glutamine (300 μg/mL), penicillin (100 U/mL), and streptomycin (100 U/mL) at a temperature of 37 °C in a humidified environment with 5% CO_2. The cells were seeded in 96-well plates at a density of 1×10^4 cells per well, and the samples were then incubated at 37 °C for 24 h. Subsequently, both cell lines were exposed to different concentrations of QU drug, UiO-66-NH_2, Fe_3O_4-COOH, Fe_3O_4-COOH@UiO-66-NH_2, and QU@Fe_3O_4-COOH@UiO-66-NH_2 for a duration of 48 h. Each treatment group was replicated at least thrice, and a control group was cultured under identical conditions without any added agents. After the incubation period, MTT solution (final concentration of 0.05 mg/well) was added to each well and incubated for 4 h. Afterward, dimethyl sulfoxide (DMSO) was used for dissolving the formazan crystals formed inside the cells, with 100 μL of DMSO added to each well. The absorbance was measured at 570 nm through an ELISA reader, and the cell viability percentages were calculated relative to the control group. The inhibitory concentration (IC_{50}) values for each treatment group were calculated utilizing nonlinear regression analysis.

2.6. Cellular Uptake Study. As the QU drug shows intrinsic green fluorescence, the cellular uptake of QU@Fe_3O_4@UiO-66-NH_2 was tracked by fluorescence microscopy. For this purpose, the 2×10^5 MDA-MB-231 cells were seeded into each well of the 6-well plates and incubated for 24 h. Then, cells were treated with 192 μg/mL QU@Fe_3O_4@UiO-66-NH_2 for the next 24 h. This concentration was the IC_{50} value achieved in the MTT assay step. Following incubation, the cells were treated with trypsin and, subsequently, centrifuged at a speed of 1500 rpm for a duration of 5 min. Following that, the cells were washed three times for 3 min and stained with DAPI at 37 °C for 10 min in the dark. In the end, the cells were investigated by using fluorescence microscopy. Afterward, a thorough washing procedure was performed on the cells, three times for 3 min. Following the washes, the cells were subjected to DAPI staining in a dark environment at 37 °C for a duration of 10 min. Subsequently, fluorescence microscopy was applied to examine and analyze the cells.

2.7. Determining the Cell Death Mechanism. The Annexin V-FITC/PI staining kit (Apoptosis detection kit, Roche, Germany) was used to investigate the mechanism of cell death induced by QU, UiO-66-NH_2, Fe_3O_4@UiO-66-NH_2, and QU@Fe_3O_4@UiO-66-NH_2. For this purpose, the 3×10^5 MDA-MB-231 cells/well were seeded for 24 h and then

https://doi.org/10.1021/acsomega.3c04863
ACS Omega 2023, 8, 41321−41338

exposed to the IC_{50} concentrations of QU@Fe_3O_4@UiO-66-NH_2 (192 μg/mL). In accordance with company guidelines, after being washed with PBS (ice-cold), cells were stained with Annexin V-FITC (5 μL) and PI 10 μL and then incubated in the dark (10 min, 25 °C). Ultimately, flow cytometry analysis was performed on the cells. The obtained histograms for each group of the cells were analyzed using FlowJo software (version 7.6).

2.8. Statistical Analysis. The statistical analysis of the relative cell viability percentage data was conducted by using Prism 8.0 software. The Kruskal–Wallis test, followed by Dunn's multiple comparison test, was employed for the analysis. In all statistical evaluations, a significance level of $*p \leq 0.05$ was utilized to determine the presence of significant differences between the control and treatment groups.

3. RESULTS AND DISCUSSION

3.1. Synthesis and Characterization. Magnetic nanocarrier of Fe_3O_4-COOH@UiO-66-NH_2 with core–shell nanospheres was fabricated based on Fe_3O_4 nanoparticles as a magnetic core via a layer-by-layer strategy. Initially, carboxylic acid-modified Fe_3O_4 (Fe_3O_4-COOH) nanospheres were prepared employing a facile one-pot solvothermal method by reduction of $FeCl_3$ with EG, as both the solvent and reducing agent, in the presence of sodium acetate, as an alkali source, and Na_3Cit, as a biocompatible electrostatic stabilizer. Citrate attachment on magnetite nanocrystal surfaces is promoted by the three carboxylate groups in Na_3Cit which have a great affinity to Fe(III) ions, preventing them from aggregating into larger crystals. Moreover, Na_3Cit is mainly used as a food additive, usually for flavor or as a preservative. In the following step, the Fe_3O_4-COOH@UiO-66-NH_2 core–shell nanocomposite was prepared via the LBL approach by combining zirconium precursor ($Zr_6O_4(OH)_4(OMc)_{12}$) as a metal-ion source and 2-aminobenzene-1,4-dicarboxylic acid as an organic bridging ligand by employing the sonochemical synthesis at room temperature. Conventional approaches involve acidic reagents ($ZrCl_4$, $ZrOCl_2$, and HCl) under solvothermal conditions including high temperatures and pressures. However, zirconium propoxide, $Zr(OPr)_4$, offers an attractive alternative for $ZrCl_4$ and $ZrOCl_2$ in UiO-66-NH_2 synthesis since it requires no harsh conditions such as high temperatures and pressures. Magnetic Fe_3O_4-COOH nanoparticles are utilized as a magnetic core with a shell comprising UiO-66-NH_2. The synthetic procedure is illustrated in Scheme 1. Quercetin, as an anticancer drug, was loaded into the Fe_3O_4-COOH@UiO-66-NH_2 core–shell composite to explore the impact of the magnetic nanoparticle-based nanocarrier on the drug delivery efficiency of quercetin. A comprehensive description of the synthesis procedure is presented in the Experimental Section.

Powder X-ray diffraction (PXRD) analysis was applied to evaluate the crystallinities and compositions of the synthesized materials (Figure 1). A comparative analysis was performed between the PXRD pattern of the Zr precursor and the simulated pattern, as depicted in Figure 1a. The observed significant similarity confirmed the successful synthesis of the Zr precursor. The Fe_3O_4-COOH pattern demonstrated excellent agreement with the Fe_3O_4 reference pattern found in the Powder Diffraction File (PDF) standard card (JCPDS card number 19-0629) and exhibited typical reflections of Fe_3O_4. Fe_3O_4-COOH@UiO-66-NH_2 illustrated the typical reflections of UiO-66-NH_2 and Fe_3O_4 confirming the growth

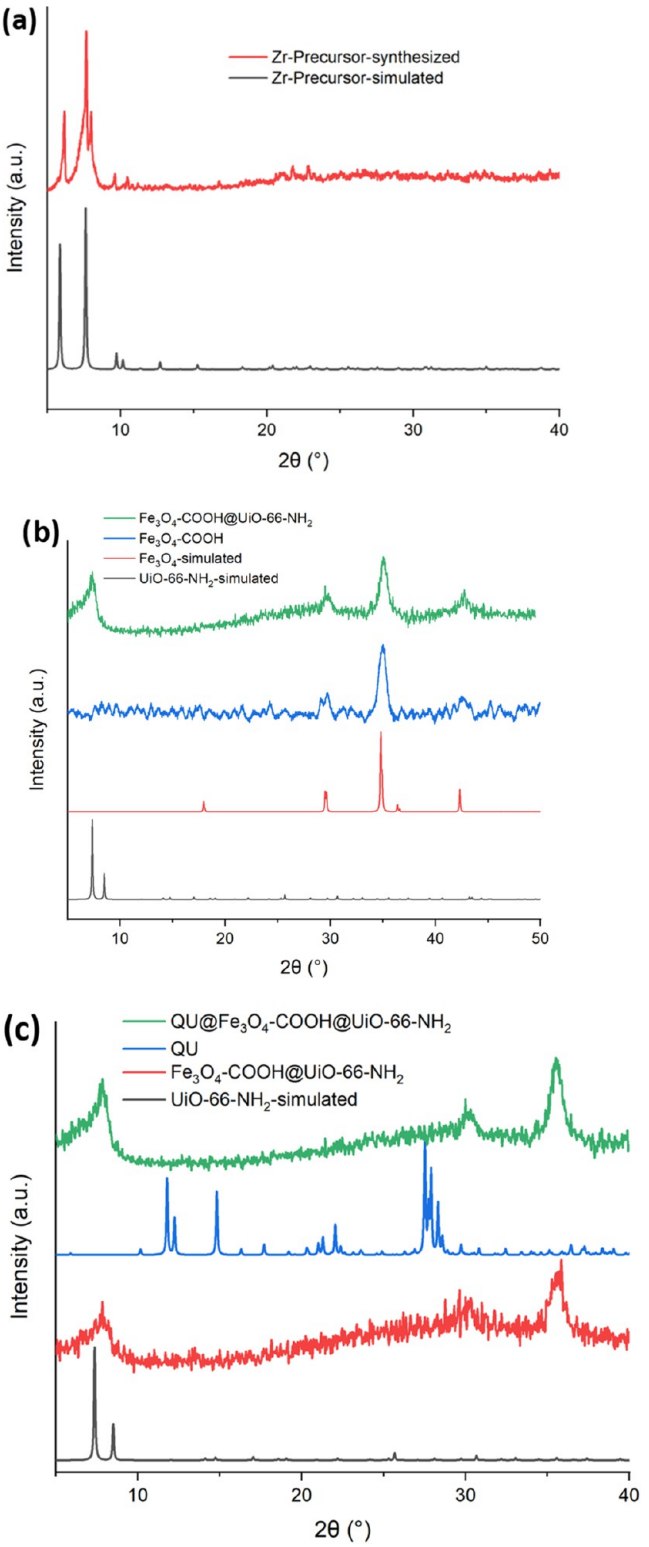

Figure 1. PXRD patterns of (a) Zr precursor ($Zr_6O_4(OH)_4(OMc)_{12}$); (b) Fe_3O_4-COOH@UiO-66-NH_2 and Fe_3O_4-COOH; and (c) Fe_3O_4-COOH@UiO-66-NH_2, QU, and QU@Fe_3O_4-COOH@UiO-66-NH_2 compared to simulated patterns.

of UiO-66-NH_2 on magnetic nanoparticle surfaces (Figure 1b). The observed broadening of the peak widths can be attributed to the existence of nanoparticles within the sample.[155] The drug-loaded sample, QU@Fe_3O_4-COOH@UiO-66-NH_2, exhibited good agreement with the UiO-66-NH_2 PXRD pattern

https://doi.org/10.1021/acsomega.3c04863
ACS Omega 2023, 8, 41321−41338

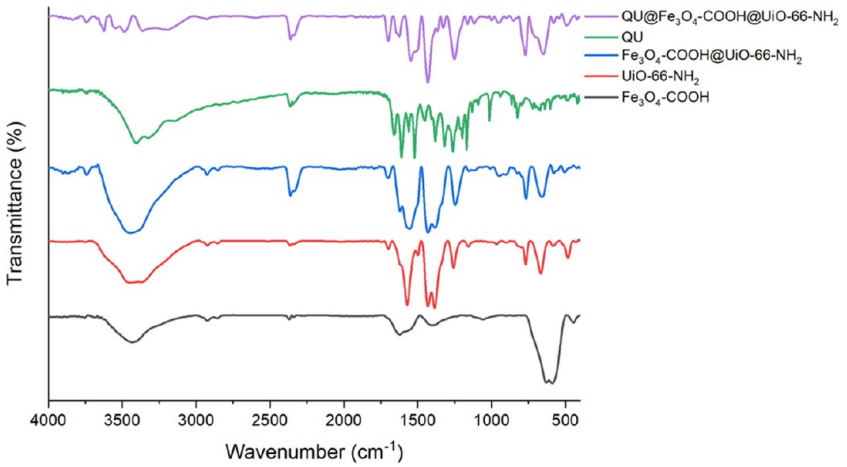

Figure 2. FT-IR spectrum of Fe_3O_4-COOH, UiO-66-NH_2, Fe_3O_4-COOH@UiO-66-NH_2, pure QU, and QU@Fe_3O_4-COOH@UiO-66-NH_2.

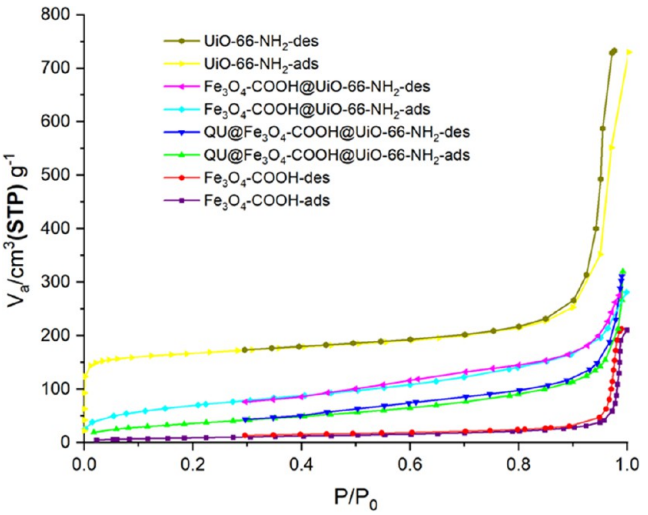

Figure 3. Nitrogen adsorption−desorption isotherms of Fe_3O_4-COOH, Fe_3O_4-COOH@UiO-66-NH_2, and QU@Fe_3O_4-COOH@UiO-66-NH_2.

Table 1. Surface Area and Pore Volume of Fe_3O_4-COOH, UiO-66-NH_2, Fe_3O_4-COOH@UiO-66-NH_2, and QU@Fe_3O_4-COOH@UiO-66-NH_2

sample	S_{BET} (m^2/g)	pore volume ($cm^3\ g^{-1}$)
Fe_3O_4-COOH	33.4	0.02
UiO-66-NH_2	648.1	1.02
Fe_3O_4-COOH@UiO-66-NH_2	251.1	0.45
QU@Fe_3O_4-COOH@UiO-66-NH_2	133.6	0.18

(Figure 1c). In addition, QU incorporation did not affect the crystal structure of Fe_3O_4-COOH@UiO-66-NH_2. Furthermore, the PXRD pattern of the drug-loaded sample did not contain the same peaks as those in the PXRD pattern of the QU, demonstrating that the drug had not crystallized within the nanoparticle pores or surfaces. Therefore, these results demonstrated that Fe_3O_4-COOH@UiO-66-NH_2 was synthesized and loaded with the drug successfully.

The FT-IR spectra of Fe_3O_4-COOH, UiO-66-NH_2, and Fe_3O_4-COOH@UiO-66-NH_2 nanoparticles are depicted in Figure 2. In the FT-IR spectrum of Fe_3O_4-COOH, the stretching vibration of the carboxylic acid O−H group is observed as a wide band spanning the range of 3100−3600 cm^{-1}. The presence of a sharp peak at 580 cm^{-1} corresponds to the Fe−O stretching vibration. Additionally, two broad peaks centered at around 1550 and 1625 cm^{-1} are assigned to symmetric and asymmetric stretches of the C═O group, respectively. The peak at 1400 cm^{-1} is related to the C−O vibrations. These results indicated the surface modification of Fe_3O_4 nanoparticles with a carboxyl group. The presence of magnetic nanoparticles in the Fe_3O_4-COOH@UiO-66-NH_2 spectrum was confirmed by the observation of a distinctive absorption peak at 580 cm^{-1}, corresponding to the Fe−O bond. The successful preparation of Fe_3O_4-COOH@UiO-66-NH_2 was further validated by the presence of characteristic absorption peaks in the spectrum. The peaks at 1386 and 1570 cm^{-1} arise from the symmetrical and asymmetrical stretching vibrations of the C═O group, respectively. The vibrations of the Zr−O bonds are reflected by the peaks observed at 485 and 670 cm^{-1}. The C−N and C−O stretching vibrations are represented by the peaks at approximately 1160 and 1258 cm^{-1}, respectively. The peaks at 1498 and 1430 cm^{-1} correspond to the C−C stretching vibrations within the aromatic rings. The stretching vibrations of the C−H bonds result in two weak peaks at 2846 and 2939 cm^{-1}. The N−H vibration is evident from the peaks detected at 3360 and 3460 cm^{-1}. Furthermore, following the drug-loading procedure, the presence of specific peaks associated with QU in the spectra confirmed the successful incorporation of the drug into the nanoparticles. In the spectrum of QU, the broad band between 3360 and 3460 cm^{-1} is attributed to the O−H vibration. The characteristic peak at 1662 cm^{-1} is related to the C═O stretching vibration. The two peaks of QU appearing at 1610 and 1520 cm^{-1} are assigned to the C═C stretching vibration. In the spectrum of QU@Fe_3O_4-COOH@UiO-66-NH_2, the broad peak of OH shifted to higher values, and its intensity also decreased as a result of quercetin incorporation. These results suggested that quercetin binds to zirconium metal through the OH group. The oxo and hydroxyl groups in quercetin facilitate the coordination and chelation of various metal ions (Figure S4 in the SI).[156] According to research, the antioxidant activity of quercetin is enhanced upon complexation with metal ions.[157−163] Furthermore, a unique characteristic of the UiO-66 family is that it is possible for up to 12 ligand units to coordinate with the metal node. As a result of this high degree of coordination, the remaining ligands

https://doi.org/10.1021/acsomega.3c04863
ACS Omega 2023, 8, 41321−41338

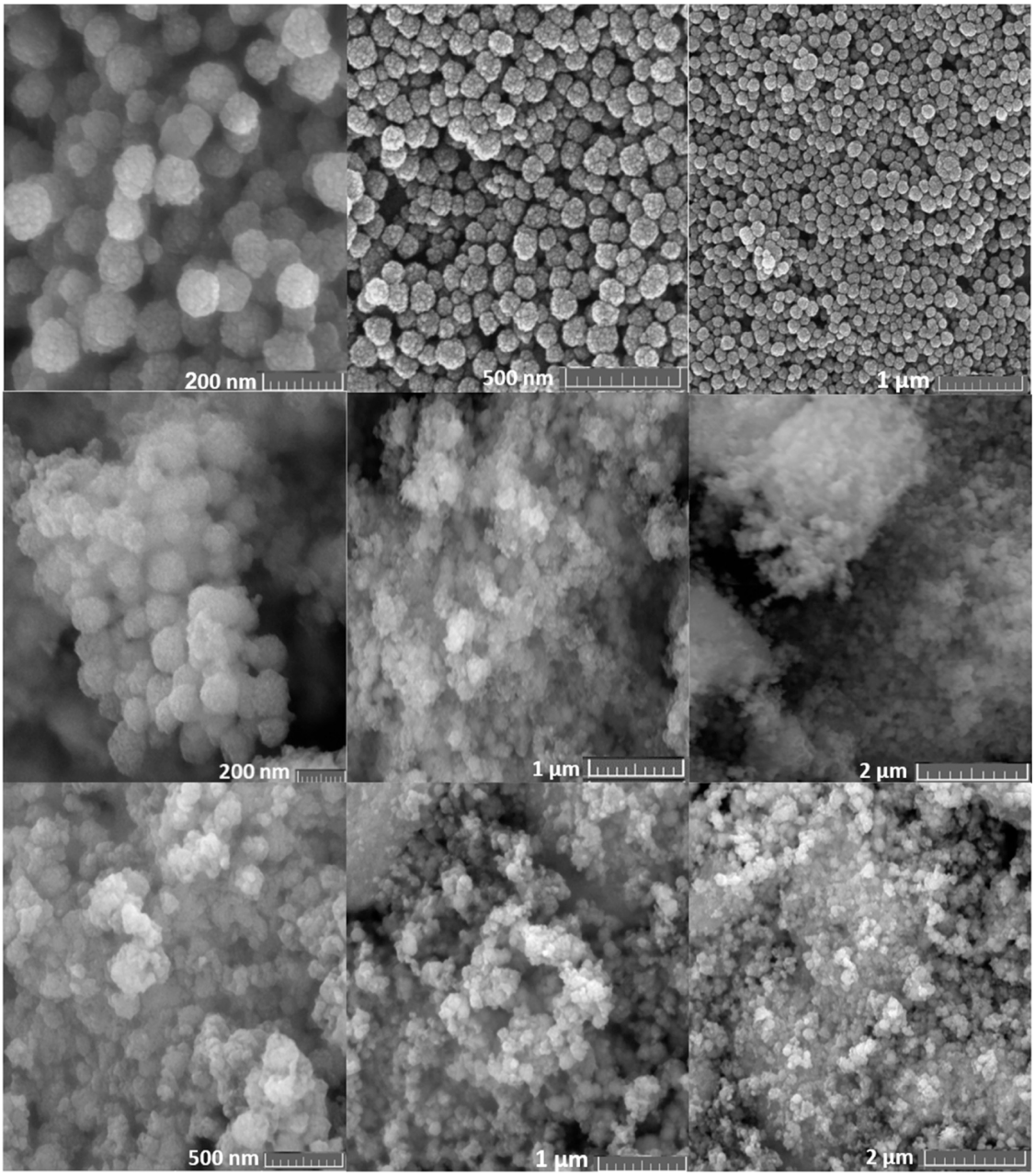

Figure 4. FE-SEM images of Fe_3O_4-COOH (top), Fe_3O_4-COOH@UiO-66-NH_2 (center), and QU@Fe_3O_4-COOH@UiO-66-NH_2 (bottom).

maintain sufficient structural integrity within the crystal, allowing for the omission of multiple ligands and resulting in the formation of structural defects. These defects introduce enhanced functionality as the absence of linkers creates vacant zirconium metal sites at the nodes, facilitating increased opportunities for drug adsorption.[164]

The porosity of the synthesized nanoparticles was assessed through N_2 adsorption−desorption isotherms, as depicted in Figure 3. The Brunauer−Emmett−Teller (BET) surface areas and pore volumes of the samples are summarized in Table 1. Fe_3O_4-COOH@UiO-66-NH_2 and QU@Fe_3O_4-COOH@UiO-66-NH_2 exhibited Type I isotherms, which indicated the presence of microporous materials according to IUPAC classification. Fe_3O_4-COOH, on the other hand, displayed a Type II isotherm, which is characteristic of nonporous materials. Subsequently, the coating of high-porosity UiO-66-NH_2 resulted in a considerable increase in the total pore volumes and BET surface areas. The BET surface area of Fe_3O_4-COOH@UiO-66-NH_2 decreased upon drug loading, confirming the successful incorporation of QU within the nanocarrier. Furthermore, a decrease in the pore volume occurred in Fe_3O_4-COOH@UiO-66-NH_2 after drug loading, signifying the inclusion of QU within the pores of UiO-66-NH_2. Consequently, the inclusion of loaded drugs in the pores of Fe_3O_4-COOH@UiO-66-NH_2 was confirmed by the observed reduction in the pore volume and BET surface area.

FE-SEM images of Fe_3O_4-COOH, Fe_3O_4-COOH@UiO-66-NH_2, and QU@Fe_3O_4-COOH@UiO-66-NH_2 are shown in Figure 4. Fe_3O_4-COOH magnetite particles (Figure 4, top) exhibited a regular spherical shape and a uniform size of about 100 nm. Fe_3O_4-COOH@UiO-66-NH_2 (Figure 4, center) illustrated spherical morphology with an average particle size of around 120 nm confirming the UiO-66-NH_2 grown on the Fe_3O_4-COOH sphere surface. QU@Fe_3O_4-COOH@UiO-66-

https://doi.org/10.1021/acsomega.3c04863
ACS Omega 2023, 8, 41321−41338

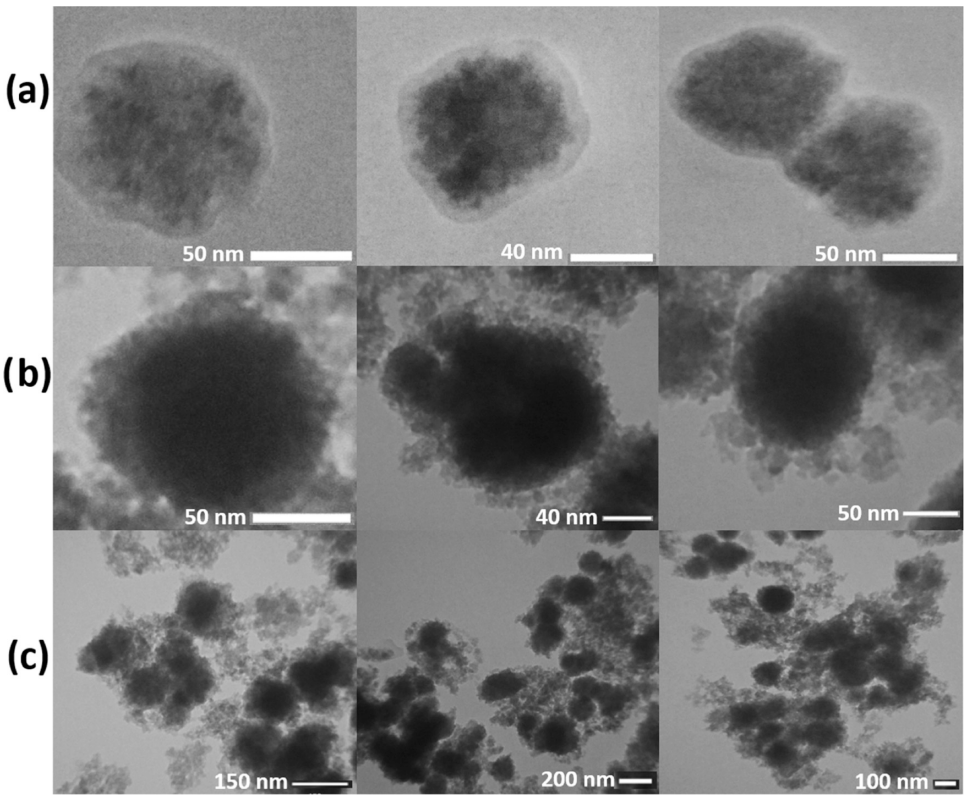

Figure 5. TEM images of (a) Fe_3O_4-COOH, (b) Fe_3O_4-COOH@UiO-66-NH_2, and (c) QU@Fe_3O_4-COOH@UiO-66-NH_2.

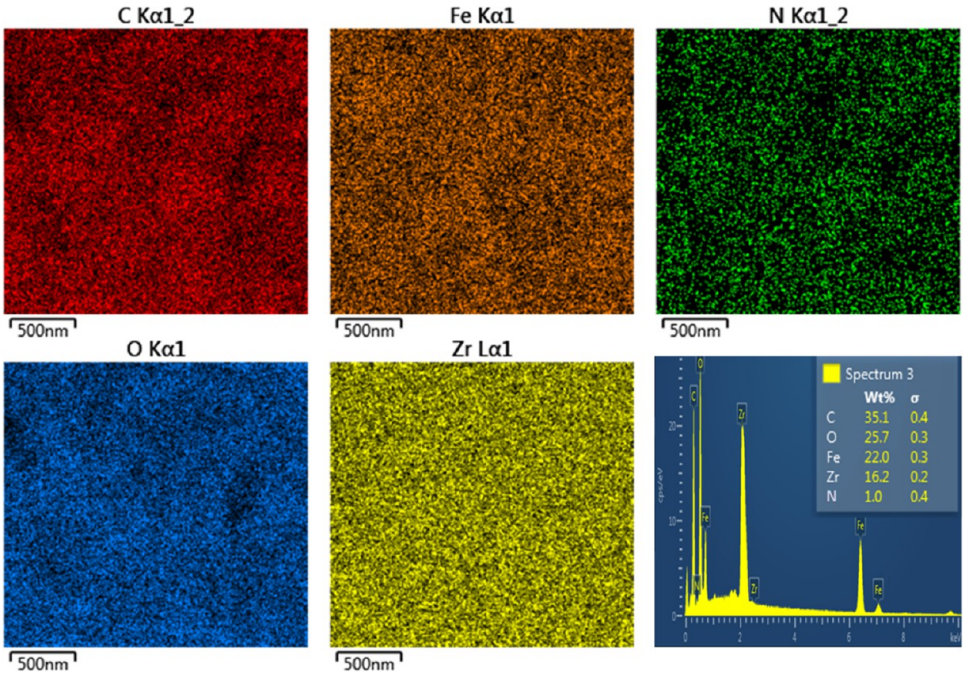

Figure 6. EDX spectra and elemental mapping for QU@Fe_3O_4-COOH@UiO-66-NH_2.

NH_2 nanoparticles (Figure 4, bottom) showed an increase in size to 140 nm after drug loading, suggesting that the drug adsorbs on the particle surface. Due to more van der Waals interactions and aggregation resulting from drug loading, QU@Fe_3O_4-COOH@UiO-66-NH_2 displayed more lumps compared with Fe_3O_4-COOH@UiO-66-NH_2. The observed morphological changes after drug loading suggest drug adsorption onto the Fe_3O_4-COOH@UiO-66-NH_2 nanoparticles surface. Compared to the reported literature, the particles became more uniform in size and shape.[154] These results are supported by the TEM images (Figure 5). TEM images confirmed the core−shell nature of Fe_3O_4-COOH nanoparticles which showed the formation of organic carboxylate shells around the Fe_3O_4 rigid material (Figure 5a). TEM images further showed spherical core−shell Fe_3O_4-COOH@UiO-66-NH_2 indicating formation of UiO-66-NH_2 shell

https://doi.org/10.1021/acsomega.3c04863
ACS Omega 2023, 8, 41321−41338

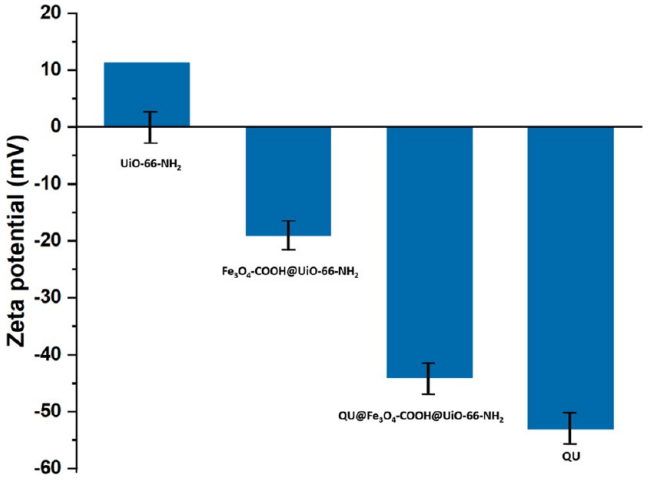

Figure 7. Zeta potential of UiO-66-NH_2, Fe_3O_4-COOH@UiO-66-NH_2, QU@Fe_3O_4-COOH@UiO-66-NH_2, and pure QU.

around the Fe_3O_4-COOH core nanoparticles (Figure 5b). The average shell thickness of UiO-66-NH_2 is approximately 20 nm (1 nm per self-assembling cycle). TEM images of QU@Fe_3O_4-COOH@UiO-66-NH_2 also illustrated the adsorbed molecules of QU on Fe_3O_4-COOH@UiO-66-NH_2 (Figure 5c). These results confirmed the adsorption of the drug onto nanocarrier surfaces as well as the accommodation in pores. The standard cancer treatment and imaging strategies maximize nanoparticle absorption at tumor sites via enhanced permeation and retention (EPR).[165] The nanoparticles between 100 and 200 nm can be passively released from tumor vessels and can penetrate tumor cells, making them ideal for achieving EPR in solid tumors while escaping the liver and spleen filtration traps.[166]

The chemical composition analysis of the QU@Fe_3O_4-COOH@UiO-66-NH_2 nanoparticles was conducted through energy-dispersive X-ray spectroscopy (EDX), as demonstrated in Figure 6. The EDX analysis demonstrated the quantitative presence of C (35.1%), O (25.7%), Fe (22.0%), Zr (16.2%), and N (1.0%). Elemental mapping demonstrated uniform distributions of elements within QU@Fe_3O_4-COOH@UiO-66-NH_2 nanoparticles (Figure 6).

The surface charge and environmental characteristics of the nanoparticles were evaluated through the measurement of zeta potentials (ZPs) which provide insights into the stability of colloidal systems (Figure 7). A ZP of 11, −19, −44, and −53 mV was measured for UiO-66-NH_2, Fe_3O_4-COOH@UiO-66-NH_2, QU@Fe_3O_4-COOH@UiO-66-NH_2, and QU, respectively. UiO-66-NH_2 demonstrated a positively charged surface due to the protonated amino group in the aqueous medium. In addition, Fe_3O_4-COOH@UiO-66-NH_2 exhibits a negative surface charge as a result of the negative carboxylate anions within the nanoparticles surface. Furthermore, the ZP value decreased after drug loading due to QU adsorption on Fe_3O_4-COOH@UiO-66-NH_2 nanoparticles surfaces. ZP of ±40 to ±60 indicates the good stability of suspended nanoparticles due to the high surface charge.[167]

To evaluate the magnetic properties of the magnetic nanocomposites, magnetic measurements were conducted at room temperature. The saturation magnetization values (Ms) of Fe_3O_4-COOH, Fe_3O_4-COOH@UiO-66-NH_2, and QU@Fe_3O_4-COOH@UiO-66-NH_2 were measured to be 69.4, 30.4, and 16.1 emu g^{-1}, respectively (Figure 8). The existence of nonmagnetic UiO-66-NH_2 reduced the magnetic property of Fe_3O_4-COOH nanoparticles. In addition, a further decrease in the magnetization value was observed after drug loading due to the presence of nonmagnetic QU drug. According to VSM plots, all prepared nanoparticles exhibited super magnetic properties. Coercive field (H_C) and remanence magnetization (M_r) are zero for superparamagnetic particles by definition.[168] Hysteresis is therefore prevented so that their residual magnetization is zero after the external magnetic field. As a result of this property, the possibility of agglomeration in vivo decreases by preventing coagulation compared to that of other magnetic nanoparticles. Due to their unique characteristics, such as biodegradability, biocompatibility, and synthesis simplicity, superparamagnetic iron oxide nanoparticles (SPIONs) have received the most research attention. Moreover, superparamagnetic nanoparticles offer better control over their application of magnetic properties due to their strong magnetic response. Because of these features, they are the most

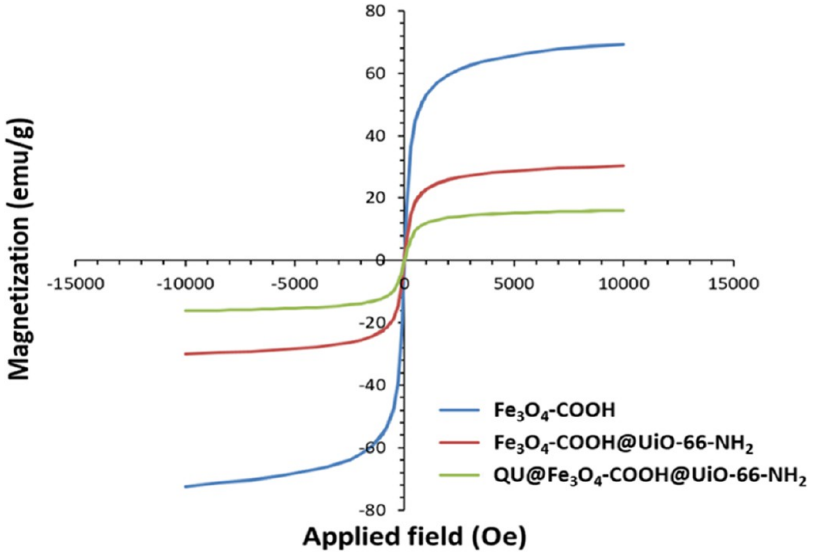

Figure 8. VSM curves of Fe_3O_4-COOH, Fe_3O_4-COOH@UiO-66-NH_2, and QU@Fe_3O_4-COOH@UiO-66-NH_2 at room temperature.

https://doi.org/10.1021/acsomega.3c04863
ACS Omega 2023, 8, 41321−41338

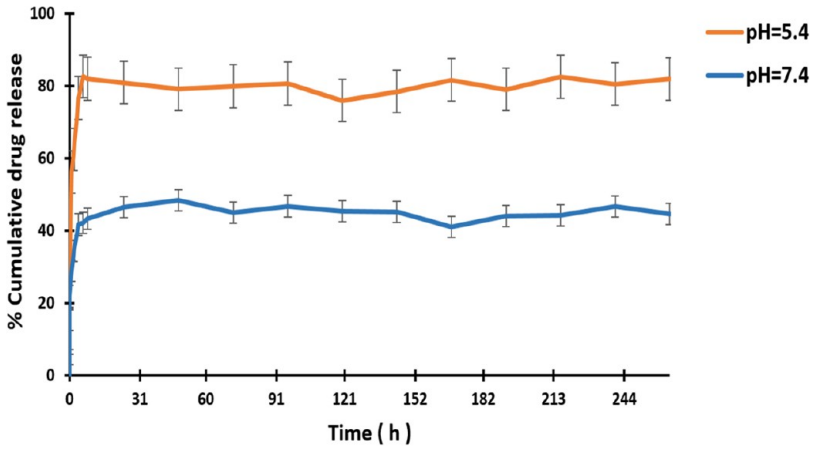

Figure 9. QU drug release profile of QU@Fe_3O_4-COOH@UiO-66-NH_2 at two pH values of 5.4 and 7.4.

appropriate types of magnetic nanoparticles for biomedical applications. In the biomedical field, SPIONs are used for many applications. The most well-known applications are magnetic resonance imaging (MRI) as contrast agents and magnetic drug delivery as carriers.[169]

3.2. Drug Loading and Release Study. In accordance with QU's calibration curve in ethanol obtained by UV−vis spectroscopy, the amount of drug loading was determined at λ = 374 nm as a result of $\pi-\pi^*$ transitions in the enol form.[170] DLC and DLE were measured as 43.1 and 53.9%, respectively. In a recent investigation, simulation findings demonstrated the significant involvement of both hydrogen bonding and $\pi-\pi$ stacking interactions in the adsorption mechanism of quercetin within UiO-66 analogues.[74] As cancerous cells are more acidic than normal cells, different release behaviors of nanocarriers under different pH conditions lead to selectivity in tumor treatment. The in vitro drug release behavior of the prepared nanocarrier was investigated at two pH values of 7.4 for simulating the normal tissue environment and 5.4 for simulating the tumor environment using the calibration curve of QU in PBS. The results are illustrated in Figure 9. QU@Fe_3O_4-COOH@UiO-66-NH_2 exhibited a burst drug release in approximately 8 h, which was caused by the drug adsorbing on the surface of the Fe_3O_4-COOH@UiO-66-NH_2. Such burst drug release strengthens the therapeutic effects upon uptake by cancer cells.[171−173] Thereafter, the observed results indicated prolonged drug release behavior for QU@Fe_3O_4-COOH@UiO-66-NH_2 (11 days). QU@Fe_3O_4-COOH@UiO-66-NH_2 released 81% of the drug under an acidic environment within 11 days, while 44% was released under normal conditions during the same period. Therefore, the release of QU from Fe_3O_4-COOH@UiO-66-NH_2 can be triggered by acidic pH, resulting in an on-demand drug release in the tumor site.

The longevity and biodistribution of nanocarriers significantly impact their therapeutic efficacy, emphasizing the critical role of stability in their performance. Maintaining the structural integrity of nanocarriers is crucial as it directly influences their lifespan and distribution within the body. Furthermore, the effective elimination of biomedical nanoparticles is essential to prevent their accumulation in targeted tissues, thereby mitigating potential long-term retention risks. Therefore, achieving an optimal balance of stability is imperative for nanocarriers, as it enables controlled degradation and clearance, ultimately reducing the risk-to-benefit ratio and minimizing bioaccumulation.[174] During the release process, QU@Fe_3O_4-COOH@UiO-66-NH_2 exhibited gradual structural degradation under acidic environments and eventually lost its entire structure due to linker protonation at lower pH.[175] In consequence, cellular accumulation will be prevented. Considering this issue, an investigation of the stability of QU@Fe_3O_4-COOH@UiO-66-NH_2 in PBS at pH = 5.4 at 37 °C was carried out. As demonstrated by the PXRD patterns (Figure S5 in the SI), QU@Fe_3O_4-COOH@UiO-66-NH_2 lost its crystal structure after long-term release, preventing nanocarrier accumulation. Additionally, the FE-SEM images of QU@Fe_3O_4-COOH@UiO-66-NH_2 illustrated changes in morphology after drug release at pH = 5.4. As shown in FE-SEM images of QU@Fe_3O_4-COOH@UiO-66-NH_2 at pH = 5.4 after 11 days of drug release, nanosized structures with different morphology were observed (Figure S6 in the SI).

3.3. Cytotoxicity Assay. The cell toxicity effects of the prepared magnetic Fe_3O_4-COOH@UiO-66-NH_2 nanoparticles alone and after QU loading against MDA-MB-231 and HEK-293 cells were assessed by using the MTT assay. Cell toxicity assessment was conducted on each component of the final product (QU@Fe_3O_4-COOH@UiO-66-NH_2) including QU, Fe_3O_4-COOH, UiO-66-NH_2, and Fe_3O_4-COOH@UiO-66-NH_2. The cytotoxicity analysis results after 48 h of incubation are illustrated in Figure 10 (a−e).

Based on the obtained results, a decreasing cell viability was observed with an increasing concentration of each component. A significant decrease in cell viability occurred in cancerous MDA-MB-231 cells treated with QU@Fe_3O_4-COOH@UiO-66-NH_2 (Figure 10e). No cytotoxicity effects were observed for the components in the HEK-293 cell line, even at high concentrations. The estimated IC_{50} values of different treatment groups are given in Table 2.

3.4. Analysis of the Cell Uptake by Fluorescence Microscopy. The cellular internalization of the QU@Fe_3O_4-COOH@UiO-66-NH_2 nanocarrier in MDA-MB-231 cells was evaluated by fluorescence microscopy imaging. As a result of the intrinsic green fluorescence potential of QU, cells that took up QU@Fe_3O_4-COOH@UiO-66-NH_2 were able to emit green fluorescence (Figure 11). The results demonstrated that the cancerous cells were capable of absorbing the QU@Fe_3O_4-COOH@UiO-66-NH_2 nanocarrier.

3.5. Cell Death Mechanism Analysis. The cell death mechanisms induced in MDA-MB-231 cells following treatment with QU, UiO-66-NH_2, Fe_3O_4-COOH@UiO-66-NH_2, and QU@Fe_3O_4-COOH@UiO-66-NH_2 were investigated

https://doi.org/10.1021/acsomega.3c04863
ACS Omega 2023, 8, 41321−41338

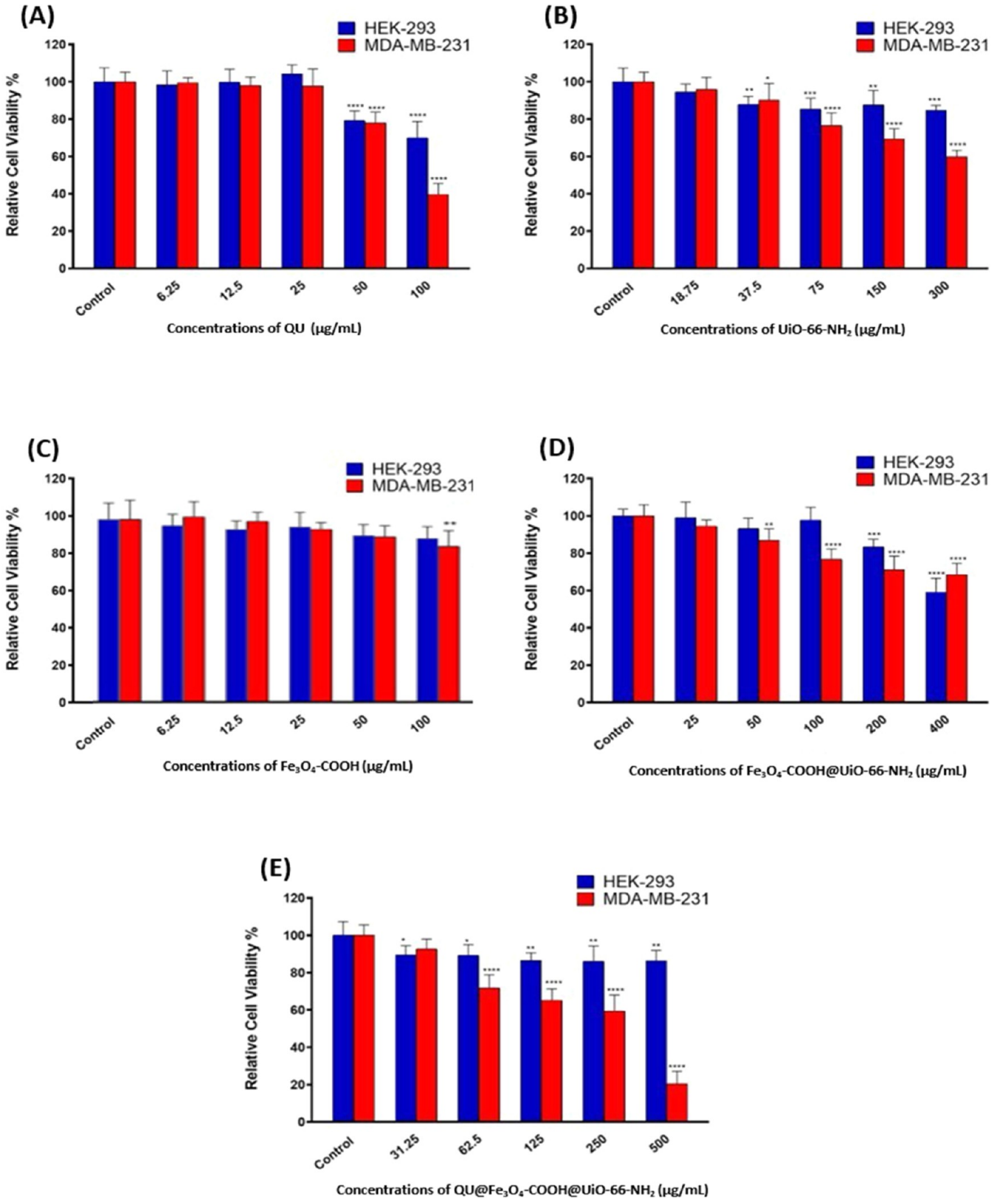

Figure 10. Cytotoxic activity of (a) QU, (b) UiO-66-NH_2, (C) Fe_3O_4-COOH, (d) Fe_3O_4-COOH@UiO-66-NH_2, and (e) QU@Fe_3O_4-COOH@UiO-66-NH_2 against normal cell lines (HEK-293) and human breast cancer cell lines (MDA-MB-231) after 48 h. The concentrations of each agent are on the X axis. The cell viability percentages are expressed relative to the control cells. Statistically significant differences between the control and treatment groups for each cell line were observed, with the corresponding significance levels denoted as ****$p \leq 0.0001$, ***$p \leq 0.001$, **$p \leq 0.01$, and *$p \leq 0.05$.

https://doi.org/10.1021/acsomega.3c04863
ACS Omega 2023, 8, 41321−41338

Table 2. Estimated IC_{50} (μg/mL) Values of Different Treatment Groups

cell lines	QU	UiO-66-NH_2	Fe_3O_4-COOH	Fe_3O_4-COOH@UiO-66-NH_2	QU@Fe_3O_4-COOH@UiO-66-NH_2
HEK-293	N.A.[a]	N.A.[a]	N.A.[a]	N.A.[a]	N.A.[a]
MDA-MB-231	129	605	N.A.[a]	N.A.[a]	192

[a]N.A = Nonaccountable.

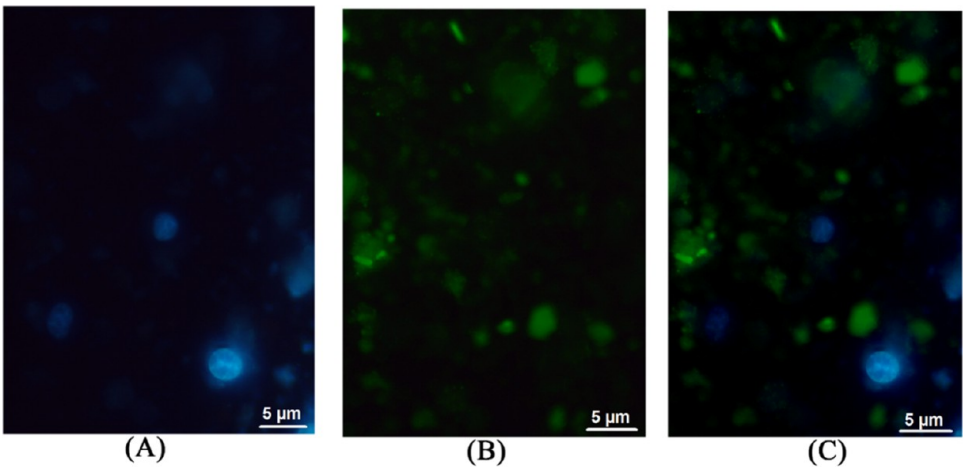

Figure 11. Fluorescence images of (a) cell nucleus (blue fluorescence, DAPI-stained), (b) QU@Fe_3O_4-COOH@UiO-66-NH_2 nanocarrier internalization into MDA-MB-231 cells (green fluorescence), and (c) overlay image (scale bars = 5 μm).

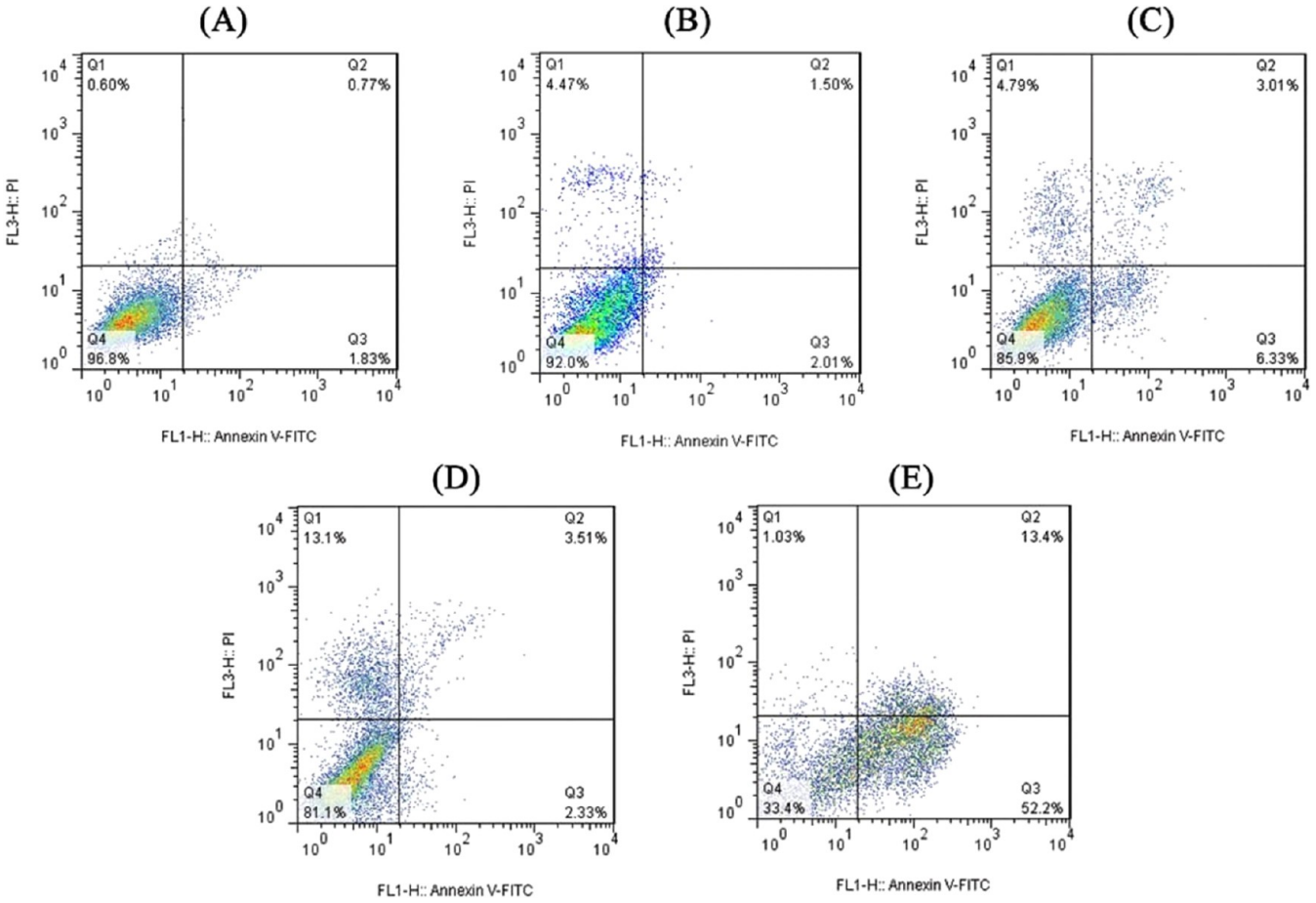

Figure 12. Flow cytometry results for determining cell death mechanisms with the Annexin V-FITC/PI double staining method. Histograms show flow cytometry analysis of MDA-MB-231 cells for (a) untreated control, (b) QU, (c) UiO-66-NH_2, (d) Fe_3O_4-COOH@UiO-66-NH_2, and (e) QU@Fe_3O_4-COOH@UiO-66-NH_2 groups. Viable, early, and late apoptotic cell populations are presented in Q4, Q3, and Q2, respectively.

https://doi.org/10.1021/acsomega.3c04863
ACS Omega 2023, 8, 41321−41338

using the Annexin V-FITC/PI double staining method. Results revealed that the population of the cells in early and late apoptotic stages (Q3+Q2) is evidently increased after exposure to QU@Fe_3O_4-COOH@UiO-66-NH_2 (Figure 12e) compared with those treated with the other groups and the nontreated control group (Figure 12a−d, respectively). Moreover, quantifying the percentage of early and late apoptotic cells (Q3+Q2) for QU, UiO-66-NH_2, and Fe_3O_4-COOH@UiO-66-NH_2 (Figure 12b−d) exhibited no significant differences. In addition, the value of (Q3+Q2) was negligible for these three groups. Also, (Q3+Q2) was 65.6% for QU@Fe_3O_4-COOH@UiO-66-NH_2, whereas 3.51% for QU. Furthermore, QU@Fe_3O_4-COOH@UiO-66-NH_2-exposed cells exhibited 1.54% necrotic death of total cell death (66.63%) compared to QU-exposed cells demonstrating 56.01% necrotic death of total cell death (7.98%). As a result of these observations, it appears that the QU@Fe_3O_4-COOH@UiO-66-NH_2 nanocarrier has the potential to induce apoptosis more effectively than each of its derivatives or even the drug individually. Therefore, the obtained data supported the idea that this nanomagnetic drug carrier could accelerate cancerous cell death through the apoptosis pathway. According to these observations, Fe_3O_4-COOH@UiO-66-NH_2 demonstrated considerable potential as a highly efficient nanocarrier for the targeted delivery of the anticancer drug QU to cancerous tumors.

4. CONCLUSIONS

In this research, QU@Fe_3O_4-COOH@UiO-66-NH_2 nanoparticles were synthesized for tumor-targeting drug delivery. A magnetic core−shell metal−organic framework (Fe_3O_4-COOH@UiO-66-NH_2) was synthesized under ambient conditions through the fabrication of an UiO-66-NH_2 shell containing a zirconium methacrylate oxo cluster as the metal source and 2-aminoterephthalic acid as the linker on the carboxylic acid-modified Fe_3O_4 surface core through a sonochemical approach. QU, as an anticancer drug, was incorporated into the magnetic core−shell nanoparticles. Characterization of the synthesized magnetic nanoparticles was carried out through various analysis methods including FT-IR, PXRD, FE-SEM, EDX, TEM, BET, UV−vis, ZP, and VSM. The drug release investigations were conducted at two values of pH (7.4 and 5.4). The resulting data indicated that QU@Fe_3O_4-COOH@UiO-66-NH_2 exhibited a high loading capacity (43.1%) and pH-controllable release behavior over a prolonged period of time (11 days). To evaluate the cytotoxicity effects of QU, UiO-66-NH_2, Fe_3O_4-COOH, Fe_3O_4-COOH@UiO-66-NH_2, and QU@Fe_3O_4-COOH@UiO-66-NH_2, MTT assays were performed on HEK-293 as the normal cell line and MDA-MB-231 as the human breast cancer cell line. Based on the results, MDA-MB-231 cancer cells treated with QU@Fe_3O_4-COOH@UiO-66-NH_2 exhibited a significant decrease in viability. Moreover, the cellular uptake and cell death mechanisms were investigated. According to the results, the QU@Fe_3O_4-COOH@UiO-66-NH_2 nanomagnetic drug carrier was taken up by cancerous cells and induced cancerous cell death through the apoptosis pathway. The QU@Fe_3O_4-COOH@UiO-66-NH_2 nanocarrier demonstrated several beneficial properties such as facile and inexpensive manufacturing process, good stability, high loading capacity, large pore size and high surface area, low cytotoxicity against normal cells, and pH-controllable release over an extended duration, which introduced it as a highly promising drug delivery system with substantial potential.

ASSOCIATED CONTENT

Supporting Information

The Supporting Information is available free of charge at https://pubs.acs.org/doi/10.1021/acsomega.3c04863.

Structure of quercetin (Figure S1), calibration curves of quercetin in ethanol and PBS (Figures S2 and S3), chelating sites of quercetin (Figure S4), optimization of ferric salt and trisodium citrate concentrations (Table S1), PXRD patterns (Figure S5), and FE-SEM images (Figure S6) (PDF)

AUTHOR INFORMATION

Corresponding Author

Kamran Akhbari − *School of Chemistry, College of Science, University of Tehran, 14155-6455 Tehran, Iran;* orcid.org/0000-0002-4574-683X; Email: akhbari.k@ut.ac.ir

Author

Mozhgan Parsaei − *School of Chemistry, College of Science, University of Tehran, 14155-6455 Tehran, Iran*

Complete contact information is available at: https://pubs.acs.org/10.1021/acsomega.3c04863

Notes

The authors declare no competing financial interest.

ACKNOWLEDGMENTS

The authors express their gratitude to the University of Tehran for their support in conducting this study through grant number 01/1/389845.

REFERENCES

(1) Nam, J. S.; Sharma, A. R.; Nguyen, L. T.; Chakraborty, C.; Sharma, G.; Lee, S. S. Application of Bioactive Quercetin in Oncotherapy: From Nutrition to Nanomedicine. *Molecules* **2016**, *21* (1), No. E108.

(2) Davis, J. M.; Murphy, E. A.; Carmichael, M. D. Effects of the Dietary Flavonoid Quercetin Upon Performance and Health. *Curr. Sports Med. Rep.* **2009**, *8* (4), 206−213.

(3) Havsteen, B. Flavonoids, a class of natural products of high pharmacological potency. *Biochem. Pharmacol.* **1983**, *32*, 1141−1148.

(4) Cyboran, S.; Bonarska-Kujawa, D.; Pruchnik, H.; Żyłka, R.; Oszmiański, J.; Kleszczyńska, H. Phenolic content and biological activity of extracts of blackcurrant fruit and leaves. *Food Res. Int.* **2014**, *65*, 47−58.

(5) Russo, M.; Spagnuolo, C.; Tedesco, I.; Bilotto, S.; Russo, G. L. The flavonoid quercetin in disease prevention and therapy: facts and fancies. *Biochem. Pharmacol.* **2012**, *83*, 6−15.

(6) Dajas, F. Life or death: neuroprotective and anticancer effects of quercetin. *J. Ethnopharmacol.* **2012**, *143* (2), 383−396.

(7) Zhang, J.; Shen, L.; Li, X.; Song, W.; Liu, Y.; Huang, L. Nanoformulated Codelivery of Quercetin and Alantolactone Promotes an Antitumor Response through Synergistic Immunogenic Cell Death for Microsatellite-Stable Colorectal Cancer. *ACS Nano* **2019**, *13* (11), 12511−12524.

(8) Wang, Y.; Tao, B.; Wan, Y.; Sun, Y.; Wang, L.; Sun, J.; Li, C. Drug delivery based pharmacological enhancement and current insights of quercetin with therapeutic potential against oral diseases. *Biomed. Pharmacother.* **2020**, *128*, No. 110372.

(9) Shah, P. M.; Priya, V. V.; Gayathri, R. Quercetin-a flavonoid: a systematic review. *J. Pharm. Sci.* **2016**, *8* (8), 878−880.

(10) Harwood, M.; Danielewska-Nikiel, B.; Borzelleca, J. F.; Flamm, G. W.; Williams, G. M.; Lines, T. C. A critical review of the data related to the safety of quercetin and lack of evidence of in vivo

toxicity, including lack of genotoxic/carcinogenic properties. *Food Chem. Toxicol.* **2007**, *45* (11), 2179−2205.
(11) Caddeo, C.; Gabriele, M.; Fernàndez-Busquets, X.; Valenti, D.; Fadda, A. M.; Pucci, L.; Manconi, M. Antioxidant activity of quercetin in Eudragit-coated liposomes for intestinal delivery. *Int. J. Pharm.* **2019**, *565*, 64−69.
(12) Piovezana Bossolani, G. D.; Silva, B. T.; Colombo Martins Perles, J. V.; Lima, M. M.; Vieira Frez, F. C.; Garcia de Souza, S. R.; Sehaber-Sierakowski, C. C.; BersaniAmado, C. A.; Zanoni, J. N. Rheumatoid arthritis induces enteric neurodegeneration and jejunal inflammation, and quercetin promotes neuroprotective and anti-inflammatory actions. *Life Sci.* **2019**, *238*, No. 116956.
(13) Güran, M.; Şanlıtürk, G.; Kerküklü, N. R.; Altundağ, E. M.; Süha Yalçın, A. Combined effects of quercetin and curcumin on anti-inflammatory and antimicrobial parameters in vitro. *Eur. J. Pharmacol.* **2019**, *859*, No. 172486.
(14) Kundur, S.; Prayag, A.; Selvakumar, P.; Nguyen, H.; McKee, L.; Cruz, C.; Srinivasan, A.; Shoyele, S.; Lakshmikuttyamma, A. Synergistic anticancer action of quercetin and curcumin against triple-negative breast cancer cell lines. *J. Cell Physiol.* **2019**, *234* (7), 11103−11118.
(15) Alvarez-Arellano, L.; Salazar-García, M.; Corona, J. C. Neuroprotective effects of quercetin in pediatric neurological diseases. *Molecules* **2020**, *25* (23), 5597.
(16) Corrêa, R. C. G.; Peralta, R. M.; Haminiuk, C. W. I.; Maciel, G. M.; Bracht, A.; Ferreira, I. C. F. R. New phytochemicals as potential human anti-aging compounds: reality, promise, and challenges. *Crit. Rev. Food Sci. Nutr.* **2018**, *58*, 942−957.
(17) Ding, Y.; Li, C.; Zhang, Y.; Ma, P.; Zhao, T.; Che, D.; Cao, J.; Wang, J.; Liu, R.; Zhang, T.; He, L. Quercetin as a Lyn kinase inhibitor inhibits IgE-mediated allergic conjunctivitis. *Food Chem. Toxicol.* **2020**, *135*, No. 110924.
(18) Hirpara, K. V.; Aggarwal, P.; Mukherjee, A. J.; Joshi, N.; Burman, A. C. Quercetin and its derivatives: synthesis, pharmacological uses with special emphasis on anti-tumor properties and prodrug with enhanced bioavailability. *Anticancer Agents Med. Chem.* **2009**, *9* (2), 138−161.
(19) Fang, X. K.; Gao, J.; Zhu, D. N. Kaempferol and quercetin isolated from Euonymus alatus improve glucose uptake of 3T3-L1 cells without adipogenesis activity. *Life Sci.* **2008**, *82*, 615−622.
(20) Li, K.; Zang, X.; Meng, X.; Li, Y.; Xie, Y.; Chen, X. Targeted delivery of quercetin by biotinylated mixed micelles for non-small cell lung cancer treatment. *Drug Delivery* **2022**, *29* (1), 970−985.
(21) Rauf, A.; Imran, M.; Khan, I. A.; Ur-Rehman, M.; Gilani, S. A.; Mehmood, Z.; Mubarak, M. S. Anticancer potential of quercetin: A comprehensive review. *Phytother. Res.* **2018**, *32* (11), 2109−2130.
(22) Hong, Y.; Lee, J.; Moon, H.; Ryu, C. H.; Seok, J.; Jung, Y.-S.; Ryu, J.; Baek, S. J. Quercetin Induces Anticancer Activity by Upregulating Pro-NAG-1/GDF15 in Differentiated Thyroid Cancer Cells. *Cancers* **2021**, *13* (12), 3022.
(23) Tang, S.-M.; Deng, X.-T.; Zhou, J.; Li, Q.-P.; Ge, X.-X.; Miao, L. Pharmacological basis and new insights of quercetin action in respect to its anti-cancer effects. *Biomed. Pharmacother.* **2020**, *121*, No. 109604.
(24) Russo, G. L.; Russo, M.; Castellano, I.; Napolitano, A.; Palumbo, A. Ovothiol isolated from sea urchin oocytes induces autophagy in the hep-g2 cell line. *Mar. Drugs* **2014**, *12* (7), 4069−4085.
(25) Lin, C.; Yu, Y.; Zhao, H. G.; Yang, A.; Yan, H.; Cui, Y. Combination of Quercetin with Radiotherapy Enhances Tumor Radiosensitivity in vitro and in vivo. *Radiother. Oncol.* **2012**, *104*, 395−400.
(26) Baksi, R.; Singh, D. P.; Borse, S. P.; Rana, R.; Sharma, V.; Nivsarkar, M. In vitro and in vivo anticancer efficacy potential of Quercetin loaded polymeric nanoparticles. *Biomed. Pharmacother.* **2018**, *106*, 1513−1526.
(27) Azeem, M.; Hanif, M.; Mahmood, K.; Ameer, N.; Chughtai, F. R. S.; Abid, U. An insight into anticancer, antioxidant, antimicrobial, antidiabetic and anti-inflammatory effects of quercetin: a review. *Polym. Bull.* **2022**, *80*, 241−262.
(28) Qiu, D.; Yan, X.; Xiao, X.; Zhang, G.; Wang, Y.; Cao, J.; Ma, R.; Hong, S.; Ma, M. To explore immune synergistic function of Quercetin in inhibiting breast cancer cells. *Cancer Cell Int.* **2021**, *21* (1), No. 632.
(29) Dong, Y.; Yang, J.; Yang, L.; Li, P. Quercetin Inhibits the Proliferation and Metastasis of Human Non-Small Cell Lung Cancer Cell Line: The Key Role of Src-Mediated Fibroblast Growth Factor-Inducible 14 (Fn14)/ Nuclear Factor kappa B (NF-κB) pathway. *Med. Sci. Monit.* **2020**, *26*, No. e920537.
(30) Shafabakhsh, R.; Asemi, Z. Quercetin: a natural compound for ovarian cancer treatment. *J. Ovarian Res.* **2019**, *12* (1), No. 55.
(31) Zhang, X. A.; Zhang, S.; Yin, Q.; Zhang, J. Quercetin induces human colon cancer cells apoptosis by inhibiting the nuclear factor-kappa B Pathway. *Pharmacogn. Mag.* **2015**, *11* (42), 404−409.
(32) Shen, X.; Si, Y.; Wang, Z.; Wang, J.; Guo, Y.; Zhang, X. Quercetin inhibits the growth of human gastric cancer stem cells by inducing mitochondrial-dependent apoptosis through the inhibition of PI3K/Akt signaling. *Int. J. Mol. Med.* **2016**, *38* (2), 619−626.
(33) Chen, C.; Zhou, J.; Ji, C. Quercetin: a potential drug to reverse multidrug resistance. *Life Sci.* **2010**, *87* (11−12), 333−338.
(34) Xu, W.; Xie, S.; Chen, X.; Pan, S.; Qian, H.; Zhu, X. Effects of Quercetin on the Efficacy of Various Chemotherapeutic Drugs in Cervical Cancer Cells. *Drug Des., Dev. Ther.* **2021**, *15*, 577−588.
(35) Boots, A. W.; Haenen, G. R.; Bast, A. Health effects of quercetin: from antioxidant to nutraceutical. *Eur. J. Pharmacol.* **2008**, *585*, 325−337.
(36) D'Andrea, G. Quercetin: a flavonol with multifaceted therapeutic applications? *Fitoterapia* **2015**, *106*, 256−271.
(37) Kumar, S.; Pandey, A. K. Chemistry and biological activities of flavonoids: an overview. *Sci. World J.* **2013**, *2013*, No. 162750.
(38) Ma, J. J.; Yu, Y. G.; Yin, S. W.; Tang, C. H.; Yang, X. Q. Cellular uptake and intracellular antioxidant activity of zein/chitosan nanoparticles incorporated with quercetin. *J. Agric. Food Chem.* **2018**, *66*, 12783−12793.
(39) Bonferoni, M. C.; Rossi, S.; Sandri, G.; Ferrari, F. Nanoparticle Formulations to Enhance Tumor Targeting of Poorly Soluble Polyphenols with Potential Anticancer Properties. *Semin. Cancer Biol.* **2017**, *46*, 205−214.
(40) Ratnam, D. V.; Ankola, D. D.; Bhardwaj, V.; Sahana, D. K.; Kumar, M. N. V. R. Role of Antioxidants in Prophylaxis and Therapy: A Pharmaceutical Perspective. *J. Controlled Release* **2006**, *113*, 189−207.
(41) Patra, A.; Satpathy, S.; Shenoy, A. K.; Bush, J. A.; Kazi, M.; Hussain, M. D. Formulation and evaluation of mixed polymeric micelles of quercetin for treatment of breast, ovarian, and multidrug resistant cancers. *Int. J. Nanomed.* **2018**, *13*, 2869−2881.
(42) Quagliariello, V.; Iaffaioli, R. V.; Armenia, E.; Clemente, O.; Barbarisi, M.; Nasti, G.; Berretta, M.; Ottaiano, A.; Barbarisi, A. Hyaluronic acid nanohydrogel loaded with quercetin alone or in combination to a macrolide derivative of rapamycin RAD001 (Everolimus) as a new treatment for hormone-responsive human breast cancer. *J. Cell. Physiol.* **2017**, *232*, 2063−2074.
(43) Liu, C. H.; Huang, Y. C.; Jhang, J. W.; Liu, Y. H.; Wu, W. C. Quercetin delivery to porcine cornea and sclera by solid lipid nanoparticles and nanoemulsion. *RSC Adv.* **2015**, *5*, 100923−100933.
(44) Guo, Y. J.; Yang, F.; Zhang, L.; Pi, J.; Cai, J. Y.; Yang, P. H. Facile synthesis of multifunctional germanium nanoparticles as a carrier of Quercetin to achieve enhanced biological activity. *Chem.—Asian J.* **2014**, *9*, 2272−2280.
(45) Yilmaz, M.; Karanastasis, A. A.; Chatziathanasiadou, M. V.; Oguz, M.; Kougioumtzi, A.; Clemente, N.; Kellici, T. F.; Zafeiropoulos, N. E.; Avgeropoulos, A.; Mavromoustakos, T.; Dianzani, U.; Karakurt, S.; Tzakos, A. G. Inclusion of quercetin in gold nanoparticles decorated with supramolecular hosts amplifies its tumor targeting properties. *ACS Appl. Bio Mater.* **2019**, *2*, 2715−2725.
(46) Hashemian, M.; Ghasemi-Kasman, M.; Ghasemi, S.; Akbari, A.; Moalem-Banhangi, M.; Zare, L.; Ahmadian, S. R. Fabrication and

https://doi.org/10.1021/acsomega.3c04863
ACS Omega 2023, 8, 41321−41338

evaluation of novel quercetin-conjugated FeO-β-cyclodextrin nanoparticles for potential use in epilepsy disorder. *Int. J. Nanomed.* **2019**, *14*, 6481−6495.
(47) Ramos, M. C.; Horta, B. A. C. Drug-Loading Capacity of PAMAM Dendrimers Encapsulating Quercetin Molecules: A Molecular Dynamics Study with the 2016H66 Force Field. *J. Chem. Inf. Model.* **2021**, *61* (2), 987−1000.
(48) Puoci, F.; Morelli, C.; Cirillo, G.; Curcio, M.; Parisi, O.; Maris, P.; Sisci, D.; Picci, N. Anticancer activity of a quercetin-based polymer towards HeLa cancer cells. *Anticancer Res.* **2012**, *32*, 2843−2847.
(49) Liu, P. Modification Strategies for Carbon Nanotubes as a Drug Delivery System. *Ind. Eng. Chem. Res.* **2013**, *52* (38), 13517−13527.
(50) de Oliveira Pedro, R.; Hoffmann, S.; Pereira, S.; Goycoolea, F. M.; Schmitt, C. C.; Neumann, M. G. Self-assembled amphiphilic chitosan nanoparticles for quercetin delivery to breast cancer cells. *Eur. J. Pharm. Biopharm.* **2018**, *131*, 203−210.
(51) Lakshmanan, R.; Maulik, N. Graphene-based drug delivery systems in tissue engineering and nanomedicine. *Can. J. Physiol. Pharmacol.* **2018**, *96* (9), 869−878.
(52) Trzeciak, K.; Chotera-Ouda, A.; Bak-Sypien, I. I.; Potrzebowski, M. J. Mesoporous Silica Particles as Drug Delivery Systems-The State of the Art in Loading Methods and the Recent Progress in Analytical Techniques for Monitoring These Processes. *Pharmaceutics* **2021**, *13* (7), 950.
(53) Antçnio, E.; Khalil, N. M.; Mainardes, R. M. Bovine Serum Albumin Nanoparticles Containing Quercetin: Characterization and Antioxidant Activity. *J. Nanosci. Nanotechnol.* **2016**, *16* (2), 1346−1353.
(54) Jiang, W.; Zhang, H.; Wu, J.; Zhai, G.; Li, Z.; Luan, Y.; Garg, S. CuS@MOF-Based Well-Designed Quercetin Delivery System for Chemo-Photothermal Therapy. *ACS Appl. Mater. Interfaces* **2018**, *10* (40), 34513−34523.
(55) Wong, H. L.; Bendayan, R.; Rauth, A. M.; Li, Y.; Wu, X. Y. Chemotherapy with anticancer drugs encapsulated in solid lipid nanoparticles. *Adv. Drug Delivery Rev.* **2007**, *59* (6), 491−504.
(56) Pascanu, V.; González Miera, G.; Inge, A. K.; Martín-Matute, B. Metal−Organic Frameworks as Catalysts for Organic Synthesis: A Critical Perspective. *J. Am. Chem. Soc.* **2019**, *141* (18), 7223−7234.
(57) Noori, Y.; Akhbari, K. Post-synthetic ion-exchange process in nanoporous metal−organic frameworks; an effective way for modulating their structures and properties. *RSC Adv.* **2017**, *7*, 1782−1808.
(58) Parsaei, M.; Akhbari, K.; White, J. Modulating Carbon Dioxide Storage by Facile Synthesis of Nanoporous Pillared-Layered Metal−Organic Framework with Different Synthetic Routes. *Inorg. Chem.* **2022**, *61*, 3893−3902.
(59) Salimi, S.; Akhbari, K.; Farnia, S. M. F.; White, J. M. Multiple Construction of a Hierarchical Nanoporous Manganese(II)-Based Metal−Organic Framework with Active Sites for Regulating N_2 and CO_2 Trapping. *Cryst. Growth Des.* **2022**, *22* (3), 1654−1664.
(60) Parsaei, M.; Akhbari, K.; Kawata, S. Computational Simulation of CO_2/CH_4 Separation on a Three-Dimensional Cd-Based Metal−Organic Framework. *Cryst. Growth Des.* **2023**, *23* (8), 5705−5718.
(61) Zamani Isfahani, M.; Akhbari, K.; Soltani, S.; Phuruangrat, A. Be safe against bacteria with nano CuBDC metal-organic framework loaded on silk fibers. *Mater. Chem. Phys.* **2022**, *290*, No. 126582.
(62) Achmann, S.; Hagen, G.; Kita, J.; Malkowsky, I. M.; Kiener, C.; Moos, R. Metal-organic frameworks for sensing applications in the gas phase. *Sensors* **2009**, *9* (3), 1574−1589.
(63) Soltani, S.; Akhbari, K.; Phuruangrat, A. Incorporation of silver nanoparticles on Cu-BTC metal−organic framework under the influence of reaction conditions and investigation of their antibacterial activity. *Appl. Organomet. Chem.* **2022**, *36* (6), No. e6634.
(64) Lawson, H. D.; Walton, S. P.; Chan, C. Metal−Organic Frameworks for Drug Delivery: A Design Perspective. *ACS Appl. Mater. Interfaces* **2021**, *13* (6), 7004−7020.
(65) Karimi Alavijeh, R.; Akhbari, K. Biocompatible MIL-101 (Fe) as a smart carrier with high loading potential and sustained release of curcumin. *Inorg. Chem.* **2020**, *59* (6), 3570−3578.
(66) Parsaei, M.; Akhbari, K. MOF-801 as a Nanoporous Water-Based Carrier System for in Situ Encapsulation and Sustained Release of 5-FU for Effective Cancer Therapy. *Inorg. Chem.* **2022**, *61* (15), 5912−5925.
(67) Karimi Alavijeh, R.; Akhbari, K. Improvement of curcumin loading into a nanoporous functionalized poor hydrolytic stable metal-organic framework for high anticancer activity against human gastric cancer AGS cells. *Colloids Surf., B* **2022**, *212*, No. 112340.
(68) Ke, F.; Yuan, Y. P.; Qiu, L. G.; Shen, Y. H.; Xie, A. J.; Zhu, J. F.; Tianc, X. Y.; Zhangc, L. D. Facile fabrication of magnetic metaleorganic framework nanocomposites for potential targeted drug delivery. *J. Mater. Chem.* **2011**, *21* (11), 3843−3848.
(69) Tai, S.; Zhang, W.; Zhang, J.; Luo, G.; Jia, Y.; Deng, M.; Ling, Y. Facile preparation of UiO-66 nanoparticles with tunable sizes in a continuous flow microreactor and its application in drug delivery. *Microporous Mesoporous Mater.* **2016**, *220*, 148−154.
(70) Sun, Y.; Zheng, L.; Yang, Y.; Qian, X.; Fu, T.; Li, X.; Yang, Z.; Yan, H.; Cui, C.; Tan, W. Metal−Organic Framework Nanocarriers for Drug Delivery in Biomedical Applications. *Nanomicro Lett.* **2020**, *12* (1), No. 103.
(71) Jarai, B. M.; Stillman, Z.; Attia, L.; Decker, G. E.; Bloch, E. D.; Fromen, C. A. Evaluating UiO-66 Metal−Organic Framework Nanoparticles as Acid-Sensitive Carriers for Pulmonary Drug Delivery Applications. *ACS Appl. Mater. Interfaces* **2020**, *12* (35), 38989−39004.
(72) Ma, T.; Liu, Y.; Wu, Q.; Luo, L.; Cui, Y.; Wang, X.; Chen, X.; Tan, L.; Meng, X. Quercetin-Modified Metal−Organic Frameworks for Dual Sensitization of Radiotherapy in Tumor Tissues by Inhibiting the Carbonic Anhydrase IX. *ACS Nano* **2019**, *13* (4), 4209−4219.
(73) Jiang, W.; Zhang, H.; Wu, J.; Zhai, G.; Li, Z.; Luan, Y.; Garg, S. CuS@MOF-Based Well-Designed Quercetin Delivery System for Chemo−Photothermal Therapy. *ACS Appl. Mater. Interfaces* **2018**, *10* (40), 34513−34523.
(74) Parsaei, M.; Akhbari, K. Smart Multifunctional UiO-66 Metal-Organic Framework Nanoparticles with Outstanding Drug-Loading/Release Potential for Targeted Delivery of Quercetin. *Inorg. Chem.* **2022**, *61* (37), 14528−14543.
(75) Das, S. S.; Bharadwaj, P.; Bilal, M.; Barani, M.; Rahdar, A.; Taboada, P.; Bungau, S.; Kyzas, G. Z. Stimuli-Responsive Polymeric Nanocarriers for Drug Delivery, Imaging, and Theragnosis. *Polymers* **2020**, *12* (6), 1397.
(76) Ray Chowdhuri, A.; Bhattacharya, D.; Sahu, S. K. Magnetic nanoscale metal organic frameworks for potential targeted anticancer drug delivery, imaging and as an MRI contrast agent. *Dalton Trans.* **2016**, *45* (7), 2963−2973.
(77) Rieter, W. J.; Taylor, K. M. L.; An, H.; Lin, W.; Lin, W. Nanoscale Metal−Organic Frameworks as Potential Multimodal Contrast Enhancing Agents. *J. Am. Chem. Soc.* **2006**, *128* (28), 9024−9025.
(78) Chen, G.; Yu, B.; Lu, C.; Zhang, H.; Shen, Y.; Cong, H. Controlled synthesis of Fe_3O_4@ ZIF-8 nanoparticles for drug delivery. *CrystEngComm* **2018**, *20* (46), 7486−7491.
(79) Cai, W.; Wang, J.; Chu, C.; Chen, W.; Wu, C.; Liu, G. Metal-Organic Framework-Based Stimuli-Responsive Systems for Drug Delivery. *Adv. Sci.* **2019**, *6* (1), No. 1801526.
(80) Oggianu, M.; Monni, N.; Mameli, V.; Cannas, C.; Ashoka Sahadevan, S.; Mercuri, M. L. Designing Magnetic NanoMOFs for Biomedicine: Current Trends and Applications. *Magnetochemistry* **2020**, *6* (3), 39.
(81) Osterrieth, J. W. M.; Fairen-Jimenez, D. Metal−Organic Framework Composites for Theragnostics and Drug Delivery Applications. *Biotechnol. J.* **2021**, *16* (2), No. 2000005.
(82) Peller, M.; Böll, K.; Zimpel, A.; Wuttke, S. Metal−organic framework nanoparticles for magnetic resonance imaging. *Inorg. Chem. Front.* **2018**, *5* (8), 1760−1779.
(83) Mertz, D.; Sandre, O.; Bégin-Colin, S. Drug releasing nanoplatforms activated by alternating magnetic fields. *Biochim. Biophys. Acta, Gen. Subj.* **2017**, *1861* (6), 1617−1641.

https://doi.org/10.1021/acsomega.3c04863
ACS Omega 2023, 8, 41321−41338

(84) Kumar, C. S.; Mohammad, F. Magnetic nanomaterials for hyperthermia-based therapy and controlled drug delivery. *Adv. Drug Delivery Rev.* **2011**, *63* (9), 789−808.
(85) Verkhovskii, R.; Ermakov, A.; Sindeeva, O.; Prikhozhdenko, E.; Kozlova, A.; Grishin, O.; Makarkin, M.; Gorin, D.; Bratashov, D. Effect of Size on Magnetic Polyelectrolyte Microcapsules Behavior: Biodistribution, Circulation Time, Interactions with Blood Cells and Immune System. *Pharmaceutics* **2021**, *13* (12), 2147.
(86) Yang, F.; Zhang, X.; Song, L.; Cui, H.; Myers, J.; Tingting, B.; Zhou, Y.; Chen, Z.; Ning, G. Controlled Drug Release and Hydrolysis Mechanism of Polymer−Magnetic Nanoparticle Composite. *ACS Appl. Mater. Interfaces* **2015**, *7* (18), 9410−9419.
(87) Ganguly, S.; Margel, S. Design of Magnetic Hydrogels for Hyperthermia and Drug Delivery. *Polymers* **2021**, *13* (23), 4259.
(88) Zheng, J.; Bi, J.; Zhao, W.; Sohail, M.; Fu, N.; Zhang, X. Fabrication of pH-sensitive magnetic metal-organic framework for controlled-release of heparin. *Colloids Surf., B* **2022**, *216*, No. 112555.
(89) Hashemzadeh, A.; Amerizadeh, F.; Asgharzadeh, F.; Drummen, G. P. C.; Hassanian, S. M.; Landarani, M.; Avan, A.; Sabouri, Z.; Darroudi, M.; Khazaei, M. Magnetic Amine-Functionalized UiO-66 for Oxaliplatin Delivery to Colon Cancer Cells: In Vitro Studies. *J. Clust. Sci.* **2022**, *33* (5), 2345−2361.
(90) Decoste, J. B.; Peterson, G. W.; Jasuja, H.; Glover, T. G.; Huang, Y. G.; Walton, K. S. Stability and Degradation Mechanisms of Metal-Organic Frameworks Containing the $Zr_6O_4(OH)_4$ Secondary Building Unit. *J. Mater. Chem. A* **2013**, *1* (18), 5642−5650.
(91) Orellana-Tavra, C.; Baxter, E. F.; Tian, T.; Bennett, T. D.; Slater, N. K. H.; Cheetham, A. K.; Fairen-Jimenez, D. Amorphous Metal-Organic Frameworks for Drug Delivery. *Chem. Commun.* **2015**, *51* (73), 13878−13881.
(92) Wang, T. C.; Bury, W.; Gómez-Gualdrón, D. A.; Vermeulen, N. A.; Mondloch, J. E.; Deria, P.; Zhang, K.; Moghadam, P. Z.; Sarjeant, A. A.; Snurr, R. Q.; Stoddart, J. F.; Hupp, J. T.; Farha, O. K. Ultrahigh surface area zirconium MOFs and insights into the applicability of the BET theory. *J. Am. Chem. Soc.* **2015**, *137*, 3585−3591.
(93) Kalidindi, S. B.; Nayak, S.; Briggs, M. E.; Jansat, S.; Katsoulidis, A. P.; Miller, G. J.; Warren, J. E.; Antypov, D.; Corà, F.; Slater, B.; Prestly, M. R.; Martí-Gastaldo, C.; Rosseinsky, M. J. Chemical and Structural Stability of Zirconium-based Metal−Organic Frameworks with Large Three-Dimensional Pores by Linker Engineering. *Angew. Chem., Int. Ed.* **2015**, *54*, 221−226.
(94) Furukawa, H.; Gandara, F.; Zhang, Y.-B.; Jiang, J.; Queen, W. L.; Hudson, M. R.; Yaghi, O. M. Water adsorption in porous metal−organic frameworks and related materials. *J. Am. Chem. Soc.* **2014**, *136* (11), 4369−4381.
(95) Cavka, J. H.; Jakobsen, S.; Olsbye, U.; Guillou, N.; Lamberti, C.; Bordiga, S.; Lillerud, K. P. A New Zirconium Inorganic Building Brick Forming Metal Organic Frameworks with Exceptional Stability. *J. Am. Chem. Soc.* **2008**, *130*, 13850−13851.
(96) Wang, X.; Zhou, X.; Yang, K.; Li, Q.; Wan, R.; Hu, G.; Ye, J.; Zhang, Y.; He, J.; Gu, H.; Yang, Y.; Zhu, L. Peroxidase-and UV-triggered oxidase mimetic activities of the UiO-66-NH_2/chitosan composite membrane for antibacterial properties. *Biomater. Sci.* **2021**, *9* (7), 2647−2657.
(97) Kirakci, K.; Bůžek, D.; Peer, P.; Liška, V.; Mosinger, J.; Křížová, I.; Kloda, M.; Ondrušová, S.; Lang, K.; Demel, J. Polymeric Membranes Containing Iodine-Loaded UiO-66 Nanoparticles as Water-Responsive Antibacterial and Antiviral Surfaces. *ACS Appl. Nano Mater.* **2022**, *5* (1), 1244−1251.
(98) Zhu, J.; Qiu, W.; Yao, C.; Wang, C.; Wu, D.; Pradeep, S.; Yu, J.; Dai, Z. Water-stable zirconium-based metal-organic frameworks armed polyvinyl alcohol nanofibrous membrane with enhanced antibacterial therapy for wound healing. *J. Colloid Interface Sci.* **2021**, *603*, 243−251.
(99) Zeng, Y.; Xiao, J.; Cong, Y.; Liu, J.; He, Y.; Ross, B. D.; Xu, H.; Yin, Y.; Hong, H.; Xu, W. PEGylated Nanoscale Metal−Organic Frameworks for Targeted Cancer Imaging and Drug Delivery. *Bioconjugate Chem.* **2021**, *32* (10), 2195−2204.
(100) Pourmadadi, M.; Eshaghi, M. M.; Ostovar, S.; Shamsabadipour, A.; Safakhah, S.; Mousavi, M. S.; Rahdar, A.; Pandey, S. UiO-66 metal-organic framework nanoparticles as gifted MOFs to the biomedical application: A comprehensive review. *J. Drug Delivery Sci. Technol.* **2022**, *76*, No. 103758.
(101) Abánades Lázaro, I.; Haddad, S.; Sacca, S.; Orellana-Tavra, C.; Fairen-Jimenez, D.; Forgan, R. S. Selective Surface PEGylation of UiO-66 Nanoparticles for Enhanced Stability, Cell Uptake, and pH-Responsive Drug Delivery. *Chem.* **2017**, *2* (4), 561−578.
(102) Al Neyadi, S. S.; Al Blooshi, A. G.; Nguyen, H. L.; Alnaqbi, M. A. UiO-66-NH_2 as an effective solid support for quinazoline derivatives for antibacterial agents against Gram-negative bacteria. *New J. Chem.* **2021**, *45* (43), 20386−20395.
(103) Abánades Lázaro, I.; Wells, C. J. R.; Forgan, R. S. Multivariate Modulation of the Zr MOF UiO-66 for Defect-Controlled Combination Anticancer Drug Delivery. *Angew. Chem., Int. Ed.* **2020**, *59* (13), 5211−5217.
(104) Chen, H.; Fu, Y.; Feng, K.; Zhou, Y.; Wang, X.; Huang, H.; Chen, Y.; Wang, W.; Xu, Y.; Tian, H.; Mao, Y.; Wang, J.; Zhang, Z. Polydopamine-coated UiO-66 nanoparticles loaded with perfluorotributylamine/tirapazamine for hypoxia-activated osteosarcoma therapy. *J. Nanobiotechnol.* **2021**, *19* (1), 298.
(105) Li, J.; Lu, F.; Shao, X.; You, B. 5-FU@DHA-UIO-66-NH_2 potentiates chemotherapy sensitivity of breast cancer cells through a microRNA let-7a-dependent mechanism. *Ann. Transl. Med.* **2021**, *9* (24), 1761.
(106) Ding, Q.; Xu, Z.; Zhou, L.; Rao, C.; Li, W.; Muddassir, M.; Sakiyama, H.; Li, B.; Ouyang, Q.; Liu, J. A multimodal Metal-Organic framework based on unsaturated metal site for enhancing antitumor cytotoxicity through Chemo-Photodynamic therapy. *J. Colloid Interface Sci.* **2022**, *621*, 180−194.
(107) El-Mehalmey, W. A.; Latif, N.; Ibrahim, A. H.; Haikal, R. R.; Mierzejewska, P.; Smolenski, R. T.; Yacoub, M. H.; Alkordi, M. H. Nine days extended release of adenosine from biocompatible MOFs under biologically relevant conditions. *Biomater. Sci.* **2022**, *10* (5), 1342−1351.
(108) Arafa, K. K.; Fytory, M.; Mousa, S. A.; El-Sherbiny, I. M. Nanosized biligated metal−organic framework systems for enhanced cellular and mitochondrial sequential targeting of hepatic carcinoma. *Biomater. Sci.* **2021**, *9* (19), 6609−6622.
(109) Orellana-Tavra, C.; Marshall, R. J.; Baxter, E. F.; Lázaro, I. A.; Tao, A.; Cheetham, A. K.; Forgan, R. S.; Fairen-Jimenez, D. Drug delivery and controlled release from biocompatible metal−organic frameworks using mechanical amorphization. *J. Mater. Chem. B* **2016**, *4* (47), 7697−7707.
(110) Zhao, D.; Zhang, W.; Wu, Z.-H.; Xu, H. Nanoscale Metal−Organic Frameworks and Their Nanomedicine Applications. *Front. Chem.* **2022**, *9*, No. 834171.
(111) Wang, Y.; Yan, J.; Wen, N.; Xiong, H.; Cai, S.; He, Q.; Hu, Y.; Peng, D.; Liu, Z.; Liu, Y. Metal-organic frameworks for stimuli-responsive drug delivery. *Biomaterials* **2020**, *230*, No. 119619.
(112) Rabiee, N.; Bagherzadeh, M.; Heidarian Haris, M.; Ghadiri, A. M.; Matloubi Moghaddam, F.; Fatahi, Y.; Dinarvand, R.; Jarahiyan, A.; Ahmadi, S.; Shokouhimehr, M. Polymer-Coated NH_2-UiO-66 for the Codelivery of DOX/pCRISPR. *ACS Appl. Mater. Interfaces* **2021**, *13* (9), 10796−10811.
(113) Li, L.; Han, S.; Zhao, S.; Li, X.; Liu, B.; Liu, Y. Chitosan modified metal−organic frameworks as a promising carrier for oral drug delivery. *RSC Adv.* **2020**, *10* (73), 45130−45138.
(114) Hashemzadeh, A.; Amerizadeh, F.; Asgharzadeh, F.; Darroudi, M.; Avan, A.; Hassanian, S. M.; Landarani, M.; Khazaei, M. Delivery of oxaliplatin to colorectal cancer cells by folate-targeted UiO-66-NH_2. *Toxicol. Appl. Pharmacol.* **2021**, *423*, No. 115573.
(115) Gao, X.; Cui, R.; Ji, G.; Liu, Z. Size and surface controllable metal−organic frameworks (MOFs) for fluorescence imaging and cancer therapy. *Nanoscale* **2018**, *10* (13), 6205−6211.
(116) Trushina, D. B.; Sapach, A. Y.; Burachevskaia, O. A.; Medvedev, P. V.; Khmelenin, D. N.; Borodina, T. N.; Soldatov, M. A.; Butova, V. V. Doxorubicin-Loaded Core−Shell UiO-66@SiO_2

https://doi.org/10.1021/acsomega.3c04863
ACS Omega 2023, 8, 41321−41338

Metal−Organic Frameworks for Targeted Cellular Uptake and Cancer Treatment. *Pharmaceutics* **2022**, *14* (7), 1325.
(117) Zhang, X.; Hao, X.; Qiu, S.; Lu, G.; Liu, W.; Wang, L.; Wei, Y.; Chen, B.; Lan, X.; Zhao, H. Efficient capture and release of carboxylated benzisothiazolinone from UiO-66-NH_2 for antibacterial and antifouling applications. *J. Colloid Interface Sci.* **2022**, *623*, 710−722.
(118) Li, Z.; Zhao, S.; Wang, H.; Peng, Y.; Tan, Z.; Tang, B. Functional groups influence and mechanism research of UiO-66-type metal-organic frameworks for ketoprofen delivery. *Colloids Surf., B* **2019**, *178*, 1−7.
(119) Guillerm, V.; Gross, S.; Serre, C.; Devic, T.; Bauer, M.; Férey, G. A zirconium methacrylate oxocluster as precursor for the low-temperature synthesis of porous zirconium(iv) dicarboxylates. *Chem. Commun.* **2010**, *46* (5), 767−769.
(120) Schaate, A.; Roy, P.; Godt, A.; Lippke, J.; Waltz, F.; Wiebcke, M.; Behrens, P. Modulated Synthesis of Zr-Based Metal−Organic Frameworks: From Nano to Single Crystals. *Chem.—Eur. J.* **2011**, *17* (24), 6643−6651.
(121) DeCoste, J. B.; Demasky, T. J.; Katz, M. J.; Farha, O. K.; Hupp, J. T. A UiO-66 analogue with uncoordinated carboxylic acids for the broad-spectrum removal of toxic chemicals. *New J. Chem.* **2015**, *39* (4), 2396−2399.
(122) Nandasiri, M. I.; Jambovane, S. R.; McGrail, B. P.; Schaef, H. T.; Nune, S. K. Adsorption, separation, and catalytic properties of densified metal-organic frameworks. *Coord. Chem. Rev.* **2016**, *311*, 38−52.
(123) Kim, S.-N.; Lee, Y.-R.; Hong, S.-H.; Jang, M.-S.; Ahn, W.-S. Pilot-scale synthesis of a zirconium-benzenedicarboxylate UiO-66 for CO_2 adsorption and catalysis. *Catal. Today* **2015**, *245*, 54−60.
(124) Tan, Y.; Zhang, W.; Gao, Y.; Wu, J.; Tang, B. Facile synthesis and supercapacitive properties of Zr-metal organic frameworks (UiO-66). *RSC Adv.* **2015**, *5* (23), 17601−17605.
(125) Ragon, F.; Horcajada, P.; Chevreau, H.; Hwang, Y. K.; Lee, U. H.; Miller, S. R.; Devic, T.; Chang, J.-S.; Serre, C. In Situ Energy-Dispersive X-ray Diffraction for the Synthesis Optimization and Scale-up of the Porous Zirconium Terephthalate UiO-66. *Inorg. Chem.* **2014**, *53* (5), 2491−2500.
(126) Shearer, G. C.; Chavan, S.; Ethiraj, J.; Vitillo, J. G.; Svelle, S.; Olsbye, U.; Lamberti, C.; Bordiga, S.; Lillerud, K. P. Tuned to Perfection: Ironing Out the Defects in Metal−Organic Framework UiO-66. *Chem. Mater.* **2014**, *26* (14), 4068−4071.
(127) Zlotea, C.; Phanon, D.; Mazaj, M.; Heurtaux, D.; Guillerm, V.; Serre, C.; Horcajada, P.; Devic, T.; Magnier, E.; Cuevas, F.; Férey, G.; Llewellyn, P.; Latroche, M. Effect of NH_2 and CF_3 functionalization on the hydrogen sorption properties of MOFs. *Dalton Trans.* **2011**, *40* (18), 4879−4881.
(128) Bárcia, P. S.; Guimarães, D.; Mendes, P. A. P.; Silva, J. A. C.; Guillerm, V.; Chevreau, H.; Serre, C.; Rodrigues, A. E. Reverse shape selectivity in the adsorption of hexane and xylene isomers in MOF UiO-66. *Microporous Mesoporous Mater.* **2011**, *139* (1−3), 67−73.
(129) Germann, L. S.; Katsenis, A. D.; Huskić, I.; Julien, P. A.; Užarević, K.; Etter, M.; Farha, O. K.; Friščić, T.; Dinnebier, R. E. Real-Time in Situ Monitoring of Particle and Structure Evolution in the Mechanochemical Synthesis of UiO-66 Metal−Organic Frameworks. *Cryst. Growth Des.* **2020**, *20* (1), 49−54.
(130) Kim, H.-Y.; Kim, S.-N.; Kim, J.; Ahn, W.-S. Sonochemical Synthesis of UiO-66 for CO_2 Adsorption and Xylene Isomer Separation. *Korean Chem. Eng. Res.* **2013**, *51* (4), 470−475.
(131) Wei, J.-Z.; Gong, F.-X.; Sun, X.-J.; Li, Y.; Zhang, T.; Zhao, X.-J.; Zhang, F.-M. Rapid and Low-Cost Electrochemical Synthesis of UiO-66-NH_2 with Enhanced Fluorescence Detection Performance. *Inorg. Chem.* **2019**, *58* (10), 6742−6747.
(132) Troyano, J.; Çamur, C.; Garzón-Tovar, L.; Carné-Sánchez, A.; Imaz, I.; Maspoch, D. Spray-Drying Synthesis of MOFs, COFs, and Related Composites. *Acc. Chem. Res.* **2020**, *53* (6), 1206−1217.
(133) Vo, T. K.; Le, V. N.; Yoo, K. S.; Song, M.; Kim, D.; Kim, J. Facile Synthesis of UiO-66(Zr) Using a Microwave-Assisted Continuous Tubular Reactor and Its Application for Toluene Adsorption. *Cryst. Growth Des.* **2019**, *19* (9), 4949−4956.
(134) Armstrong, M. R.; Senthilnathan, S.; Balzer, C. J.; Shan, B.; Chen, L.; Mu, B. Particle size studies to reveal crystallization mechanisms of the metal organic framework HKUST-1 during sonochemical synthesis. *Ultrason. Sonochem.* **2017**, *34*, 365−370.
(135) Masoomi, M. Y.; Bagheri, M.; Morsali, A. Porosity and dye adsorption enhancement by ultrasonic synthesized Cd(II) based metal-organic framework. *Ultrason. Sonochem.* **2017**, *37*, 244−250.
(136) Lestari, W. W.; Arvinawati, M.; Martien, R.; Kusumaningsih, T. Green and facile synthesis of MOF and nano MOF containing zinc(II) and benzene 1,3,5-tri carboxylate and its study in ibuprofen slow-release. *Mater. Chem. Phys.* **2018**, *204*, 141−146.
(137) Gordon, J.; Kazemian, H.; Rohani, S. Rapid and efficient crystallization of MIL-53(Fe) by ultrasound and microwave irradiation. *Microporous Mesoporous Mater.* **2012**, *162*, 36−43.
(138) Stawowy, M.; Róziewicz, M.; Szczepańska, E.; Silvestre-Albero, J.; Zawadzki, M.; Musioł, M.; Łużny, R.; Kaczmarczyk, J.; Trawczyński, J.; Łamacz, A. The Impact of Synthesis Method on the Properties and CO_2 Sorption Capacity of UiO-66(Ce). *Catalysts* **2019**, *9* (4), 309.
(139) Zhang, Y.; Dai, T.; Zhang, F.; Zhang, J.; Chu, G.; Quan, C. Fe_3O_4@UiO-66-NH_2 core−shell nanohybrid as stable heterogeneous catalyst for Knoevenagel condensation. *Chin. J. Catal.* **2016**, *37* (12), 2106−2113.
(140) Yin, L. L.; Kong, X. Y.; Zhang, Y.; Ji, Y. Q. Facile synthesis of the magnetic metal organic framework Fe_3O_4@UiO-66-NH_2 for separation of strontium. *Biomed. Environ. Sci.* **2018**, *31* (6), 483−488.
(141) Han, Y.; Xia, L.; Zhuang, X.; Liang, Y. Integrating of metal-organic framework UiO-66-NH_2 and cellulose nanofibers mat for high-performance adsorption of dye rose Bengal. *Front. Chem. Sci. Eng.* **2022**, *16* (9), 1387−1398.
(142) Ahmadijokani, F.; Tajahmadi, S.; Haris, M. H.; Bahi, A.; Rezakazemi, M.; Molavi, H.; Ko, F.; Arjmand, M. Fe_3O_4@PAA@UiO-66-NH_2 magnetic nanocomposite for selective adsorption of Quercetin. *Chemosphere* **2021**, *275*, No. 130087.
(143) Zhang, R.; Wang, Z.; Zhou, Z.; Li, D.; Wang, T.; Su, P.; Yang, Y. Highly effective removal of pharmaceutical compounds from aqueous solution by magnetic Zr-based MOFs composites. *Ind. Eng. Chem. Res.* **2019**, *58* (9), 3876−3884.
(144) Morelli Venturi, D.; Campana, F.; Marmottini, F.; Costantino, F.; Vaccaro, L. Extensive Screening of Green Solvents for Safe and Sustainable UiO-66 Synthesis. *ACS Sustainable Chem. Eng.* **2020**, *8* (46), 17154−17164.
(145) Kalati, M.; Akhbari, K. Optimizing the metal ion release and antibacterial activity of ZnO@ZIF-8 by modulating its synthesis method. *New J. Chem.* **2021**, *45* (48), 22924−22931.
(146) Nakhaei, M.; Akhbari, K.; Davoodi, A. Biocompatible MOF-808 as an iodophor antimicrobial agent with controlled and sustained release of iodine. *CrystEngComm* **2021**, *23* (48), 8538−8545.
(147) Karimi Alavijeh, R.; Akhbari, K.; White, J. A Ca-Based Nano Bio-Coordination Polymer Providing Reversible Structural Conversion with Ability to Enhancing Cytotoxicity of Curcumin and Inducing Apoptosis in Human Gastric Cancer AGS Cells. *CrystEngComm* **2022**, *24*, 7125−7136.
(148) Soltani, S.; Akhbari, K. Facile and single-step entrapment of chloramphenicol in ZIF-8 and evaluation of its performance in killing infectious bacteria with high loading content and controlled release of the drug. *CrystEngComm* **2022**, *24* (10), 1934−1941.
(149) Soltani, S.; Akhbari, K. Cu-BTC metal−organic framework as a biocompatible nanoporous carrier for chlorhexidine antibacterial agent. *JBIC, J. Biol. Inorg. Chem.* **2022**, *27* (1), 81−87.
(150) Parsaei, M.; Akhbari, K.; Tylianakis, E.; Froudakis, G. E. Effects of Fluorinated functionalization of Linker on Quercetin Encapsulation, Release and Hela Cell Cytotoxicity of Cu-Based MOFs as Smart pH-Stimuli Nanocarriers. *Chem.—Eur. J.* **2023**, *n/a*, No. e202301630.
(151) Liu, J.; Sun, Z.; Deng, Y.; Zou, Y.; Li, C.; Guo, X.; Xiong, L.; Gao, Y.; Li, F.; Zhao, D. Highly Water-Dispersible Biocompatible

https://doi.org/10.1021/acsomega.3c04863
ACS Omega 2023, 8, 41321−41338

Magnetite Particles with Low Cytotoxicity Stabilized by Citrate Groups. *Angew. Chem., Int. Ed.* **2009**, *48*, 5875−5879.
(152) Kickelbick, G.; Schubert, U. Oxozirconium Methacrylate Clusters: $Zr_6(OH)_4O_4(OMc)_{12}$ and $Zr_4O_2(OMc)_{12}$(OMc = Methacrylate). *Chem. Ber.* **1997**, *130* (4), 473−478.
(153) Užarević, K.; Wang, T. C.; Moon, S. Y.; Fidelli, A. M.; Hupp, J. T.; Farha, O. K.; Friščić, T. Mechanochemical and Solvent-free Assembly of Zirconium-Based Metal-organic Frameworks, Oxozirconium methacrylate clusters: $Zr_6(OH)_4O_4(OMC)_{12}$ and $Zr_4O_2(OMC)_{12}$(OMC= methacrylate). *Chem. Commun.* **2016**, *52*, 2133−2136.
(154) Chen, R.; Tao, C.-a.; Zhang, Z.; Chen, X.; Liu, Z.; Wang, J. Layer-by-Layer Fabrication of Core−Shell Fe_3O_4@UiO-66-NH_2 with High Catalytic Reactivity toward the Hydrolysis of Chemical Warfare Agent Simulants. *ACS Appl. Mater. Interfaces* **2019**, *11* (46), 43156−43165.
(155) Guillerm, V.; Gross, S.; Serre, C.; Devic, T.; Bauer, M.; Férey, G. A zirconium methacrylate oxocluster as precursor for the low-temperature synthesis of porous zirconium(IV) dicarboxylates. *Chem. Commun.* **2010**, *46* (5), 767−769.
(156) Kasprzak, M. M.; Erxleben, A.; Ochocki, J. Properties and applications of flavonoid metal complexes. *RSC Adv.* **2015**, *5* (57), 45853−45877.
(157) De Souza, R. F. V.; De Giovani, W. F. Antioxidant properties of complexes of flavonoids with metal ions. *Redox Rep.* **2004**, *9* (2), 97−104.
(158) Dehghan, G.; Khoshkam, Z. Tin(II)−quercetin complex: synthesis, spectral characterisation and antioxidant activity. *Food Chem.* **2012**, *131* (2), 422−426.
(159) Bodini, M. E.; Copia, G.; Tapia, R.; Leighton, F.; Herrera, L. Iron complexes of quercetin in aprotic medium. Redox chemistry and interaction with superoxide anion radical. *Polyhedron* **1999**, *18* (17), 2233−2239.
(160) Dimitrić Marković, J. M.; Marković, Z. S.; Brdarić, T. P.; Pavelkić, V. M.; Jadranin, M. B. Iron complexes of dietary flavonoids: combined spectroscopic and mechanistic study of their free radical scavenging activity. *Food Chem.* **2011**, *129* (4), 1567−1577.
(161) Mutlu Gençkal, H.; Erkisa, M.; Alper, P.; Sahin, S.; Ulukaya, E.; Ari, F. Mixed ligand complexes of Co(II), Ni(II) and Cu(II) with quercetin and diimine ligands: synthesis, characterization, anti-cancer and anti-oxidant activity. *JBIC, J. Biol. Inorg. Chem.* **2020**, *25*, 161−177.
(162) Chen, W.; Sun, S.; Cao, W.; Liang, Y.; Song, J. Antioxidant property of quercetin−Cr(III) complex: the role of Cr(III) ion. *J. Mol. Struct.* **2009**, *918* (1−3), 194−197.
(163) Bratu, M.; Birhila, S.; Miresan, H.; Negreanu-Pirjol, T.; Prajitur, C.; Calinescu, M. Biological activities of Zn(II) and Cu(II) complexes with quercetin and rutin: antioxidant properties and UV-Protection capacity. *Rev. Chim.* **2014**, *65*, 544−549.
(164) Winarta, J.; Shan, B.; Mcintyre, S. M.; Ye, L.; Wang, C.; Liu, J.; Mu, B. A decade of UiO-66 research: a historic review of dynamic structure, synthesis mechanisms, and characterization techniques of an archetypal metal−organic framework. *Cryst. Growth Des.* **2020**, *20* (2), 1347−1362.
(165) Oltra, N. S.; Nair, P.; Discher, D. E. From stealthy polymersomes and filomicelles to "self" peptide-nanoparticles for cancer therapy. *Annu. Rev. Chem. Biomol. Eng.* **2014**, *5*, 281.
(166) Longmire, M.; Choyke, P. L.; Kobayashi, H. Clearance properties of nano-sized particles and molecules as imaging agents: considerations and caveats. *Nanomedicine* **2008**, *3* (5), 703−717.
(167) Yu, W.; Xie, H. A Review on Nanofluids: Preparation, Stability Mechanisms, and Applications. *J. Nanomater.* **2012**, *2012*, No. 435873.
(168) Dennis, C. L.; Ivkov, R. Physics of heat generation using magnetic nanoparticles for hyperthermia. *Int. J. Hyperthermia* **2013**, *29* (8), 715−729.
(169) Mohammed, L.; Gomaa, H. G.; Ragab, D.; Zhu, J. Magnetic nanoparticles for environmental and biomedical applications: A review. *Particuology* **2017**, *30*, 1−14.
(170) Barvinchenko, V. N.; Lipkovskaya, N.; Fedyanina, T. Keto-Enol tautomerization of Quercetin in solutions of a cationic surfactant, miramistin. *Colloid J.* **2014**, *76* (1), 1−5.
(171) Zhang, J.; Lin, Y.; Lin, Z.; Wei, Q.; Qian, J.; Ruan, R.; Jiang, X.; Hou, L.; Song, J.; Ding, J.; Yang, H. Stimuli-Responsive Nanoparticles for Controlled Drug Delivery in Synergistic Cancer Immunotherapy. *Adv. Sci.* **2022**, *9* (5), No. 2103444.
(172) Huang, X.; Brazel, C. S. On the importance and mechanisms of burst release in matrix-controlled drug delivery systems. *J. Controlled Release* **2001**, *73* (2−3), 121−136.
(173) Wang, L.; Chang, M.-W.; Ahmad, Z.; Zheng, H.; Li, J.-S. Mass and controlled fabrication of aligned PVP fibers for matrix type antibiotic drug delivery systems. *Chem. Eng. J.* **2017**, *307*, 661−669.
(174) Milewska, S.; Niemirowicz-Laskowska, K.; Siemiaszko, G.; Nowicki, P.; Wilczewska, A. Z.; Car, H. Current Trends and Challenges in Pharmacoeconomic Aspects of Nanocarriers as Drug Delivery Systems for Cancer Treatment. *Int. J. Nanomedicine* **2021**, *16*, 6593−6644.
(175) Jarai, B. M.; Stillman, Z.; Attia, L.; Decker, G. E.; Bloch, E. D.; Fromen, C. A. Evaluating UiO-66 Metal-Organic Framework Nanoparticles as Acid-Sensitive Carriers for Pulmonary Drug Delivery Applications. *ACS Appl. Mater. Interfaces* **2020**, *12* (35), 38989−39004.

https://doi.org/10.1021/acsomega.3c04863
ACS Omega 2023, 8, 41321−41338